Development of a Single Particle Tracking Microscope for the Study of Nanoparticle Diffusion

A Thesis

Presented to

the faculty of the School of Engineering and Applied Science

University of Virginia

In partial fulfillment

of the requirements for the degree

Master of Science in Chemical Engineering

by

Drew William Bundschuh

August 2014

APPROVAL SHEET

The thesis

is submitted in partial fulfillment of the requirements

for the degree of

Master of Science

AUTHOR

The thesis has been read and approved by the examining committee:

Giorgio Carta

Advisor

Roseanne Ford

Kyle Lampe

Accepted for the School of Engineering and Applied Science:

Dean, School of Engineering and Applied Science

August

2014

Print Form

Abstract

Transport of nanoparticles, including proteins in stationary phases used for chromatography is controlled by diffusion. Our understanding of diffusion in such systems is based almost exclusively on macroscopic and microscopic scale measurements. Our knowledge is especially limited when transport is coupled to interactions with the matrix. Macroscopic and microscopic-scale measurements provide ensemble-averaged information, but offer little detail on the movement of individual nanoparticles. Therefore, a nanoscopic-scale measurement about the transport of individual nanoparticles is desirable. In this thesis, a single particle tracking microscope was developed to determine the movement of individual nanoparticles in solution. The tracking microscope used a total internal reflection fluorescence microscope with laser light illumination to measure the movement of individual fluorescent nanoparticles through water and glycerol solutions. Observations of Brownian motion were used to determine experimental diffusion coefficients, which were compared to diffusion coefficients calculated with the theoretical Stokes-Einstein equation. The experimental diffusion coefficients were comparable to the theoretical values, and therefore, support the use of the tracking microscope for the measurement the diffusion of molecules both in solution and polymer gel matrices used for chromatography.

Acknowledgements

I would like to thank many people who have helped me through my graduate school experience. First, I have always considered myself incredibly fortunate to have Dr. Giorgio Carta as my advisor. I greatly appreciate his valuable and constructive recommendations during this research project. Moreover, his insight has helped me define my career interest in the field of Bioseparations. I would also like to thank Gordon Laurie and the Biotechnology Training Program for their funding and for helping me realize my potential as a scientist. This project would not be possible without the funding from the Biotechnology Training Program and the National Institute of Health (Award Number T32GM008715), and the National Science Foundation, (Award Number CBET-1032727).

I would like to thank the Chemical Engineering Department at the University of Virginia for their support and guidance. I would also like to thank the current and past members of the Carta lab that have helped me numerous times: Ernie Perez-Almodovar, Tarl Vetter, Joe Basconi, Yige Wu, Shaojie Zhang, Mimi Zhu, Jing Guo, Frank Bartnik, Rachel Corbett, Arch Creasy and Jason Reck. Acknowledgements also go out to Dr. Roseanne Ford for the microscopy table, Ricky Buchanan for all the custom parts for the microscope, and Dr. Volker Kiessling and Dr. Lukas Tamm in the Molecular Physiology and Biological Physics department for their helpful knowledge of total internal reflection fluorescence microscopy.

Finally, I want to thank my friends for making my time in Charlottesville unforgettable, and my grandparents, parents, and brother for their support and encouragement throughout my study.

Table of Contents

List of Figures

List of Tables

List of Symbols

A	Area of the image (μm^2)
C	Nanosphere concentration (g/mL)
D	Diffusion coefficient (cm^2/s)
D_{BM}	Diffusion coefficient derived from observed Brownian motion (cm^2/s)
D_{SE}	Diffusion coefficient estimated from the Stokes-Einstein equation (cm^2/s)
D_{sphere}	Diameter of the sphere (μm)
d	Penetration depth of evanescent wave (nm)
$e_{\Delta t}^2$	Errors of the MSD at each time step (cm^2)
I	Intensity of the evanescent wave (kW/cm^2)
i	An individual displacement occurring during Δt (i = 1,2,3,…N)
J	Flux (g/cm^2s)
$\langle J \rangle$	Ensemble average of some property J
k_B	Boltzmann constant (J/K)
M	Total number of states within an ensemble
MSD	Average mean squared displacement (cm^2)
N	Total number of displacements occurring during Δt
n	Refractive index
r	Radius of the nanoparticle (nm)

$\vec{r}(t)$	Position vector at time *t* (cm)
T	Temperature (K)
z	Axial position (nm)
$\langle z^2(n)\rangle$	Average mean squared displacement (cm^2)
δ	Step size of particle in Brownian motion (nm)
Δt	Time interval (s)
θ	Angle of incidence (degrees)
θ_c	Critical angle determined from Snell's Law (degrees)
λ	Wavelength of the incident light in a vacuum (nm)
μ	Viscosity of the solution (cP)
ρ	Density of the polystryrene spheres (g/mL)
τ	Time step (s)
v	Velocity of a particle during one step in Brownian motion (nm/s)

1. Introduction

Nanoparticle transport is important in many fields of application. An important example is protein transport in polymer gels used for chromatographic processes. Polymer gels are composed of polymer chains crosslinked to create a tangled network immersed in a liquid medium. The crosslinked network prevents the liquid from flowing away while the liquid prevents the gel from collapsing (Tanaka, 1981). In hydrogels, water is the liquid phase holding up the hydrophilic polymer network. Hydrogels are frequently used in protein chromatography and other bioseparation processes because of their compatibility with bioproducts and their ability to separate molecules with different physiochemical properties. Neutral gels are used in electrophoresis and size exclusion chromatography as they capitalize on the ability of the hydrogel to restrict the diffusive movements of the protein molecule by reducing the average free volume per molecule available for the protein (Amsden, 1998).

Charged gels are used in ion exchange chromatography to separate different protein molecules based on both steric and electrostatic interactions (Carta and Jungbauer, 2010; Jungbauer, 2005). Such gels are often incorporated within a rigid porous support matrix made, for example, of silica or zirconia. The resultant composite material has a high mechanical strength while preserving the desirable characteristic of the hydrogel. Various examples of such composites have been shown to have both improved protein binding capacity and adsorption kinetics (Jungbauer, 2005).

The transport of proteins in ion exchange chromatography is controlled by diffusion within the stationary phase. While transport in open-pore materials is well understood, protein diffusion in gel-composite materials is not. Previous research has been conducted to understand specific features of transport phenomena in these matrices. Lewus and Carta (2001) studied the

diffusion and partitioning of cytochrome c, a cationic protein, in an anionic polyacrylamide-based hydrogel. The heme group in cytochrome c is a strong chromophore, which allowed for the visualization of concentration profiles under visible light. Russell et al. (2003) viewed the diffusion and partitioning of anionic fluorescently-labeled myoglobin in a cationic polyacrylamide-based hydrogel with fluorescence microscopy. Both studies found that the diffusion rates were higher in these gels than diffusion in water. They also discovered that the mass transfer of the protein followed a Fickian diffusion model where the flux was proportional to the adsorbed protein concentration gradient. Even though the diffusion coefficient in the gel was small compared to that in solution, the diffusive flux of the protein in the gel was much greater than in solution because favorable partitioning of the protein in the gel which generated a high driving force for mass transfer. The measurements by Lewus and Russell provided the mechanistic basis for a conceptual model of protein diffusion in charged gels but gave little molecular-scale detail of the actual mechanism.

Diffusion measurements on the microscopic scale provide ensemble-averaged information of the entire population of the diffusing species but offer little detail on the movement of individual particles. This information is critical to support both the development of molecular models and the design of more effective gel structures. Unlike the previously discussed microscopic techniques, so called, single molecule detection (SMD) techniques can identify and characterize individual particles and molecules at the nanoscopic scale (Douglass and Vale, 2008; Weiss, 1999). A frequency histogram of the measurement of individual particles can be generated, instead of ensemble-averaged measurements from microscopic or macroscopic measurements. The heterogeneities of the diffusion process can be determined from the irregularities of the distribution (Moerner and Orrit, 1999).

The SMD technique used in this project is total internal refection fluorescence (TIRF) microscopy, which is described in detail in Section 2.1 of the Background section. Although TIRF is used extensively, to our knowledge its application to protein transport in charged gels has not been considered. Thus, the overall goal of this project is to develop a TIRF microscopy system to analyze the motion of individual protein molecules in interacting with charged gels at a nanoscopic level. As a first step toward this goal, a TIRF microscope system has been designed and constructed to visualize individual fluorescently-labeled nanoparticles in solution. The diffusion coefficients of these nanoparticles are determined from their observed Brownian motion and compared with estimates based on the Stokes-Einstein equation in order to validate the technique.

The specific aims of this thesis are to:

1. Construct a TIRF-based microscope system for single nanoparticle detection;
2. Test the ability of the microscope to consistently detect the two-dimensional Brownian motion of 28 nm nanospheres in solution; and
3. Determine the nanosphere diffusivities in water and glycerol solutions and compare the results to predictions based on the Stokes-Einstein equation to validate the equipment and analysis methods.

2. Background

This section provides the theoretical background for two critical aspects of this work, (a) total internal fluorescence reflection (TIRF) microscopy and (b) models for protein diffusion.

2.1 Total Internal Fluorescence Reflection Microscopy

Fluorescence microscopy has been widely used as a tool for SMD. There are two approaches to fluorescence microscopy: scanning and widefield. Scanning fluorescence microscopy works by scanning light and collecting the fluorescence over a portion of the specimen at a time until the entire specimen is scanned. Examples of scanning microscopy include multiphoton and confocal microscopy. Widefield microscopy techniques, such as epifluorescence and total internal reflection fluorescence (TIRF) microscopy, illuminate a fixed area of a specimen and collect fluorescence through that area. Widefield techniques are better for SMD because the imaging speed of widefield techniques is not limited by the scanning system hardware or image reconstruction software that is used in scanning fluorescence microscopy (Axelrod, 2007). TIRF microscopy is well suited for this application due to its low optical penetration depth and high signal-to-noise ratio.

In TIRF microscopy, a fluorophore is excited by the evanescent wave produced when the total internal reflection of light occurs near a solid-solution interface. The emitted fluorescence is then detected, and the three-dimensional position of the fluorophore can be determined from the emitted fluorescence (Ruthardt et al., 2011). The two-dimensional position in the plane parallel to the interface is determined with particle tracking software. The position in the third dimension, normal to the interface, is determined from the known exponential decay of the

evanescent wave intensity (Axelrod, 2007). Figure 2.1 shows the mechanism for TIRF microscopy in which the evanescent wave is generated.

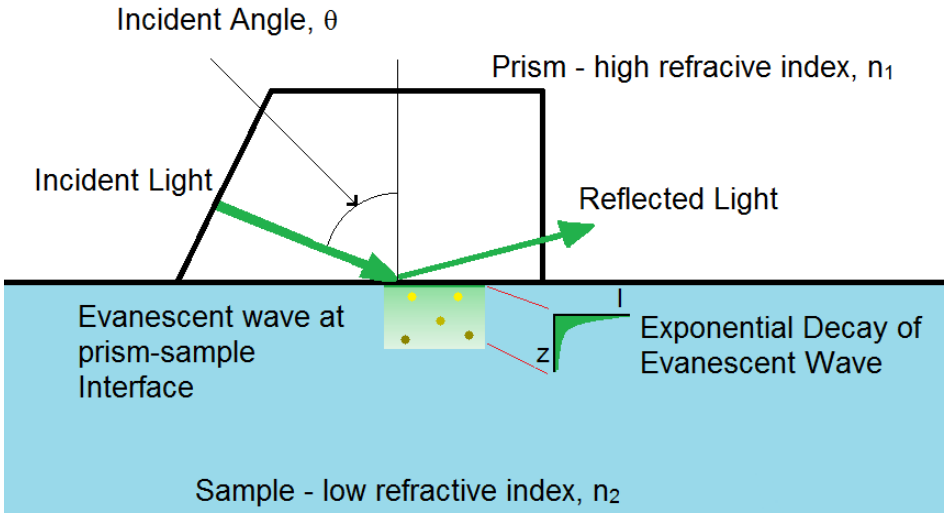

Figure 2.1. The evanescent wave is produced from the total internal reflection of light, which excites fluorophores within hundreds of nanometers away from the solid-liquid interface.

In prism-based TIRF, a prism with a high refractive index is placed over the specimen. Total internal reflection occurs when the incident angle, θ, is greater than the critical angle, θ_c, which is determined from Snell's Law as (Axelrod, 2007):

$$\theta_c = sin^{-1}\left(\frac{n_1}{n_2}\right) \tag{2.1}$$

where n_1 and n_2 are the refractive indices of phase 1 (solution) and phase 2 (solid), respectively. At these conditions, an evanescent wave is generated as a thin electromagnetic field at the solid-liquid interface with the same frequency as the incident light (Axelrod, 2001). The intensity, *I*, of the evanescent wave decays exponentially with distance *z* away from the refractive interface according to the relationship:

$$I(z) = I_o \mathrm{e}^{-z/d} \tag{2.2}$$

where I_o is the intensity (units of power/area) at $z = 0$ and d is the penetration depth, or the depth at which the intensity becomes $1/e$ of the original intensity, and is given by the following equation (Axelrod, 2001):

$$d = \frac{\lambda}{4\pi n_1}\left[\left(\frac{\sin(\theta)}{sin(\theta_c)}\right) - 1\right]^{-0.5} \tag{2.3}$$

where λ is the wavelength of the incident light in a vacuum, and θ is the angle of incidence. For practical conditions, the penetration depth is on the order of a few hundreds of nanometers. After combining Equations 2.2 and 2.3, the relationship between intensity and depth is (Born and Wolf, 1999):

$$ln\left(\frac{I}{I_o}\right) = -\frac{4\pi n_1 z}{\lambda}\left[\left(\frac{\sin(\theta)}{sin(\theta_c)}\right) - 1\right]^{0.5} \tag{2.4}$$

With this equation, assuming that the emitted fluorescence is proportional to the evanescent wave intensity, the axial position of a fluorescent nanoparticle in the evanescent wave can be determined from its brightness.

The short penetration depth is a key advantage of TIRF microscopy – fluorophores will only be illuminated if they are within the evanescent wave, thereby removing a great deal of background noise. TIRF microscopy works when two conditions are met: (1) only individual molecules are found in the focal volume and (2) the image has a large signal-to-noise ratio (Moerner and Fromm, 2003). The first condition is met by reducing the concentration of fluorophores and the focal volume of the excitation laser beam so that only individual fluorescent

molecules are seen in the focal volume. For example, approximately a 10^{-10} M concentration of fluorophores is needed for an optical volume of 10 μm^3 (Moerner and Fromm, 2003). The second condition requires the maximization of fluorescent signal and the minimization of background intensities and noise. Noise refers to the fluctuations due to detected photons and background refers to the photons that are detected by the detector from any source other than the molecule of interest. The fluorescence signal can be maximized with a stable fluorophore with a high quantum efficiency and high molar extinction coefficient (Lichtman and Conchello, 2005). The focal volume should be minimized to reduce scattered light (Moerner and Fromm 2003). Background intensity and noise can also be minimized by utilizing an optical system that includes an excitation laser with short exposure times, an objective lens with a high numerical aperture, and an electron multiplication charge-coupled device (EMCCD) camera.

The high intensity light used for excitation can lead to a phenomenon called photobleaching in which the fluorescent molecule loses its fluorescent signal (Lichtman and Conchello, 2005). The loss in signal is due to the continuous change of energy levels by the electrons which causes photon-induced chemical damage and covalent modification. The amount of fluorescence for each molecule is limited to approximately 10^6 photons at ambient conditions (Moerner and Fromm, 2003). The most common way to reduce photobleaching is to reduce the light source intensity (Lichtman and Conchello, 2005). TIRF experiments are often conducted on the timescale of milliseconds to seconds to avoid photobleaching effects.

TIRF microscopy has been used extensively for imaging biological systems. It has been used to observe actin polymerization dynamics with the regulation of proteins (Kuhn and Pollard, 2005) and to measure the adsorption of DNA, R-phycoerythrin, and bacteria with solid surfaces (Kang et al., 2001; Kang and Yeung 2002; Vigeant et al., 2002). The orientation of

molecules during adsorption on glass surfaces has been determined for lysozyme and cytochrome c (Daly et al., 2003; Bos and Kleijn, 1995). In addition, TIRF microscopy has been used to track single molecule diffusion of DNA and IgG antibody in solution (Xu and Yeung, 1997; Lieto et al., 2003), histidine kinase PleC and TGF-β in cells (Deich et al., 2004; Ma et al., 2000), and lipids in the lipid bilayer (Schmidt et al., 1995). TIRF microscopy has also been used to track Nile Red, and Rhodamine 6G through neutral polyacrylamide gels, which showed that the gel prevented Brownian motion of the molecules (Dickson et al., 1996; Kummer et al., 1998). These observations would not have been possible with conventional microscopy techniques.

2.2. Models for Diffusion

2.2.1. Stokes-Einstein Equation

An understanding of diffusional mass transfer is essential for bioseparation processes, which are generally limited by the diffusion of biomolecules. Fick's Law can be used to describe the diffusion of species *i* as a result of a concentration gradient in the absence of convection and electrostatic forces according to the following equation (Krishna and Wesselingh, 1997):

$$J = -D\frac{dC}{dz} \tag{2.5}$$

where *J* is the flux, *D* is the diffusion coefficient, *C* is the concentration, and *z* is the distance (Cussler, 2009).

It is possible to calculate the diffusion coefficients from theoretical models. The Stokes-Einstein equation is derived assuming that a rigid sphere subject to Brownian motion diffuses in a solvent without any attraction between the sphere and solvent (Cussler, 2009).

$$D_{SE} = \frac{k_B T}{6\pi\mu r} \tag{2.6}$$

where D_{SE} is the diffusion coefficient, k_B is the Boltzmann constant, T is the temperature, μ is the viscosity of the solution, and r is the radius of the solute molecule (Cussler, 2009). The Stokes-Einstein equation works best when the size of the diffusing spheres is at least five times larger than that of the solvent molecules.

2.2.2. Brownian Motion

Statistical mechanics is used to calculate macroscopic thermodynamic properties from the microscopic states and interactions. Similarly, if the nanoscopic behavior of individual nanoparticles is known, then macroscopic diffusivities can be calculated. Statistical mechanics uses ensemble averaging to measure the properties of the whole ensemble. The ensemble average is the average of the properties of individual states within the ensemble. The discrete form of the ensemble average of i individual states is:

$$\langle J \rangle = \frac{1}{M} \sum_{i=1}^{M} J_i \tag{2.7}$$

where $\langle J \rangle$ is the ensemble average of some property J and M is the total number of states within an ensemble (Carter, 2001). In this work, the mean square displacement (MSD) of each particle was ensemble averaged to determine the diffusion coefficient of the particles.

Diffusion coefficients determined from experiments are related to the random molecular motion of individual nanoparticles or molecules. A simple one-dimensional model is used to derive this relationship. The model makes three key assumptions: (1) during one step, each particle moves left or right during time step τ with a velocity v; (2) the particle has an equal

chance of moving left or right; and (3) each particle moves independently of other particles. For a system of N particles, the position, *z*, of particle *i* after *n* steps is given by:

$$z_i(n) = z_i(n-1) \pm \delta \tag{2.8}$$

where δ is the step size ($\delta = v*\tau$). The mean displacement of *N* particles after *n* steps is:

$$\langle z(n) \rangle = \frac{1}{N}\sum_{i=1}^{N} z_i(n) = \langle z(n-1) \rangle = 0 \tag{2.9}$$

The average displacement is zero because the positive and negative displacements are equally probable and cancel out. Another useful measurement to take is the variance or the spread of the particles. The variance or mean square displacement (MSD) of particle *i* is determined from the following equation:

$$z_i^2(n) = z_i^2(n-1) \pm 2\delta z_i(n-1) \pm \delta^2 \tag{2.10}$$

The average MSD is calculated with the equation:

$$\langle z^2(n) \rangle = \frac{1}{N}\sum_{i=1}^{N} z_i^2(n) = \langle z^2(n-1) \rangle + \delta^2 \tag{2.11}$$

Therefore, the average MSD of all the particles for n steps is:

$$\langle z^2(n) \rangle = n\delta^2 \tag{2.12}$$

The diffusion coefficient for a particle can be described as the path length multiplied by the velocity in a given direction. For particles with a 50% chance of moving in one direction, the diffusion coefficient is:

$$D = \frac{1}{2}\delta v \tag{2.13}$$

If $n = t/\tau$ and $v = \delta/\tau$, where t is the total time of all steps, then Equations 2.12 and 2.13 become:

$$\langle z^2(n)\rangle = n\delta^2 = \frac{t}{\tau}\delta^2 \tag{2.14}$$

$$D = \frac{1}{2}\delta v = \frac{\delta^2}{2\tau}. \tag{2.15}$$

The one-dimensional diffusion coefficient from Brownian motion can be determined by combining Equations 2.14 and 2.15:

$$\langle z^2(n)\rangle = MSD = 2Dt \tag{2.16}$$

or

$$D = \frac{MSD}{2t} \tag{2.17}$$

For two dimensions, the diffusion coefficient calculated from Brownian motion is (Cussler, 2009):

$$D = \frac{MSD}{4t} \tag{2.18}$$

Finally, for three dimensions, the diffusion coefficient is calculated as (Cussler, 2009):

$$D = \frac{MSD}{6t} \tag{2.19}$$

It can be seen that the one-dimensional, two-dimensional, and three-dimensional values of the diffusions coefficients differ only by a proportionality constant.

3. Materials and Methods

3.1. Materials

3.1.1. Nanoparticle Sample

FluoSpheres® nanoparticles obtained from Molecular Probes, Inc. (Eugene, OR) were used in this work. The nanoparticles are spherical polystyrene particles coated with carboxylic acids for the covalent coupling of biomolecules. They are labeled with Nile Red fluorescent dyes. According to the supplier, the dye density is on the order of 10^2 fluorescent equivalents/nanosphere. Nile Red, shown in Figure 3.1, has a maximum excitation at a wavelength of 535 nm and maximum emission at a wavelength of 575 nm (Molecular Probes, 2005). The nanospheres have a diameter of 28 ± 5 nm and have a slightly negative surface charge of 0.64 meq/g, as measured by Molecular Probes, due to the coated carboxylic acids.

All other chemicals used in this study were analytical reagent grade and were obtained from Fisher Scientific (Pittsburgh, PA) and Sigma-Aldrich (St. Louis, MO).

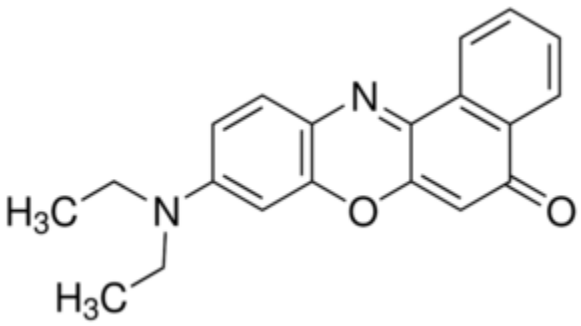

Figure 3.1. Chemical structure of Nile Red (Greenspan et al., 1985).

3.2. Methods

3.2.1 Coverslip Cleaning Preparation

In this work, a protocol for cleaning glass coverslips was adapted from Eghiaian and Schaap (2011). Equal amounts of 22 and 25 mm Fisherfinest® borosilicate coverslips (Fisher Scientific, Pittsburgh, PA) were first placed in a beaker with 0.2 M solution of NaOH. The coverslips were sonicated in this solution for 15 minutes. The coverslips were then placed in distilled water and sonicated for 5 minutes, which was repeated three times. Finally, the coverslips were dried with helium gas.

3.2.2. Nanoparticle Sample Preparation

At room temperature (22 ± 2 °C), the nanoparticles were diluted into three different solutions for imaging: (1) distilled water, (2) 80/20 (% vol.) mixture of distilled water/glycerol, and (3) 60/40 (% vol.) mixture of distilled water/glycerol. 10 μL drops of these mixtures were placed between two borosilicate coverslips, with the 22 mm coverslip on top of the 25 mm coverslip for TIRF microscopy imaging.

3.2.3. Refractive Index Measurement

The refractive indexes of the solutions were measured at room temperature with an Abbe Refractometer (Reichert, Depew, NY). The refractive indexes, viscosities at 22 °C from Cheng (2008), and the penetration depths of the evanescent wave calculated with Equation 2.3 for the solutions used in these experiments are shown in Table 3.1.

Table 3.1. Measured refractive indexes, viscosities at 22 °C, and the evanescent wave penetration depths for the solutions in these experiments.

Solvent	Refractive Index	Viscosity at 22°C (cP)*	Penetration Depth (with incident angle)**
Water	1.333	0.957	125 nm (72°)
20% vol glycerol	1.363	1.73	160 nm (72°)
40% vol glycerol	1.392	4.83	182 nm (75°)

* Viscosity values from Cheng, 2008.
** Calculated with Equation 2.3.

3.2.4. TIRF Microscope Setup

The TIRF microscopy system used for imaging is shown schematically in Figure 3.2, and photographs of the actual equipment are given in Figure 3.3. Laser illumination was supplied by a Nd:YAG diode-pumped solid-state laser (CrystaLaser®, Reno, NV) with a wavelength of 532 nm. The light traveled through a multi-mode optical fiber (CrystaLaser), which incidentally skewed or widened the beam. The light then passed through a collimator (CFC-11x-A, ThorLabs, Newton, NJ) that aligned the light into parallel waves of light and the focusing lens with a focal length of 200 mm (LA1708, ThorLabs) that focused the light towards the sample. The laser and all of the optics were held at an angle above the microscope and can be aligned in the vertical and axial directions with alignment micrometer screws.

An IX 71 S1F inverted microscope (Olympus, Center Valley, PA) equipped with a UAPON 100x oil-immersion objective lens with a numerical aperture of 1.49 also from Olympus was used to observe the fluorescent samples. The focused light passed through a quartz prism (n=1.46, obtained from CeNing Optics Co., Fujian, China). The prism was attached to a horizontal positioning arm which was lowered to place the prism on the glass coverslip sandwich containing the sample. The emitted light from the fluorescent sample traveled through the

objective and a barrier filter that allowed light with 575 ± 25 nm wavelengths (ET575/50m Chroma Technology, Bellows Falls, VT), while scattered laser light was blocked by the filter. The filtered light was detected with an iXon 879 EMCCD camera (Andor Technology, South Windsor, CT). Two-dimensional images were taken with the Andor Solis software (Andor Technology).

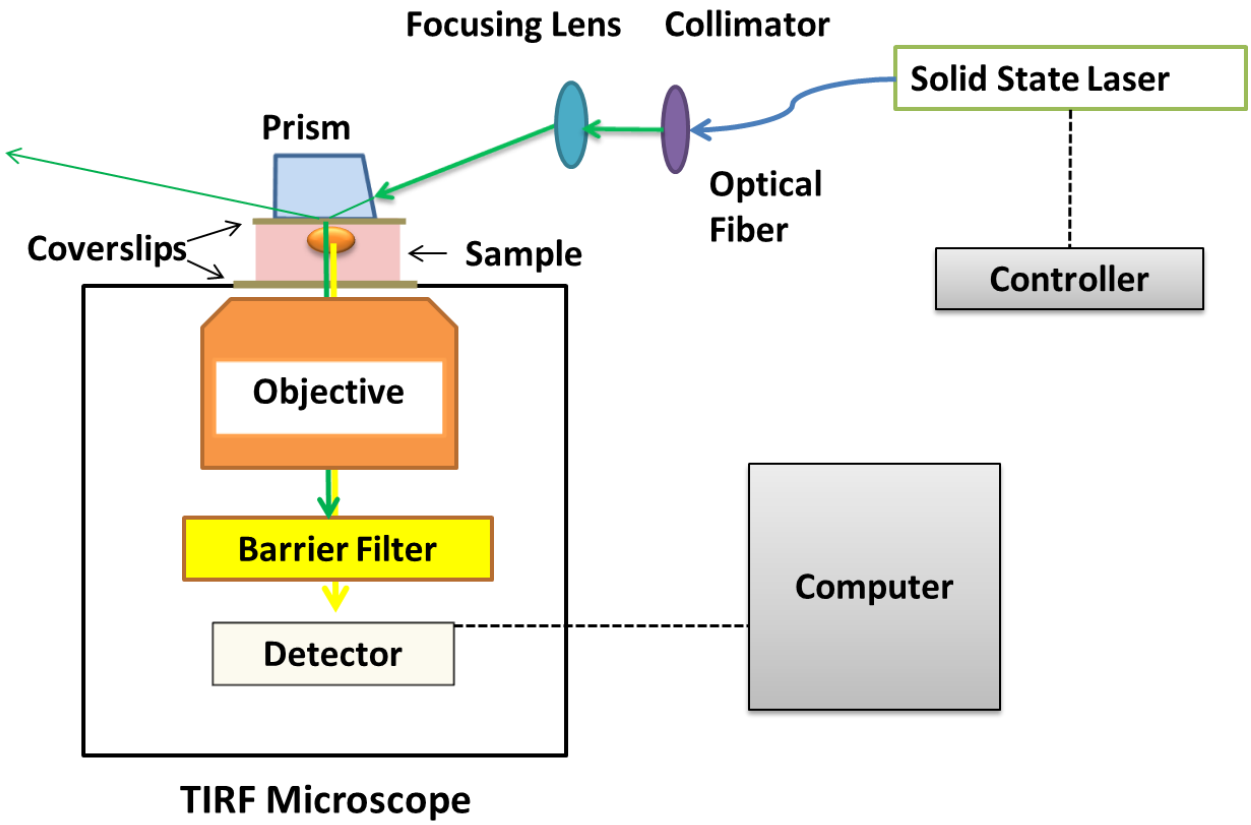

Figure 3.2. Schematic diagram of the TIRF microscopy system. Image is not to scale.

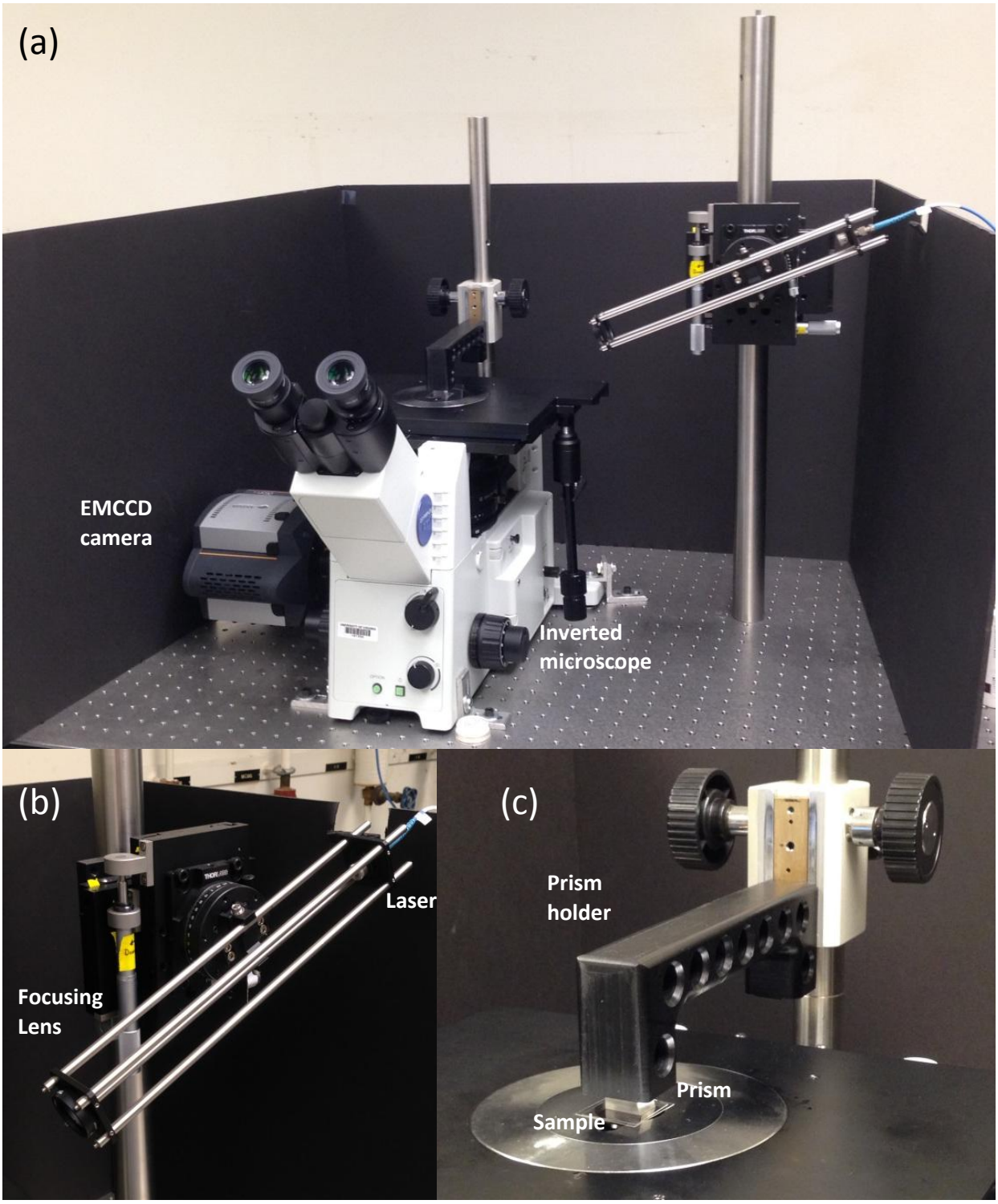

Figure 3.3. Photographs of the TIRF microscopy system. (a) The entire microscope; (b) zoomed-in view of the laser and focusing lens; and (c) the prism held on the sample with the prism holder. The laser is located behind the microscope and is coupled to the optics by an optical fiber.

3.2.5. TIRF Microscope Alignment

The microscope was aligned prior to imaging samples. The laser was set at an angle greater than the critical angle to get total internal reflection of light at the coverslip surface. The fluorescent dye of 1,1'-Dioctadecyl-3,3,3',3'-Tetramethylindocarbocyanine Perchlorate or 'DiI' (Sigma-Aldrich, St. Louis, MO) was used to align the microscope. For this purpose, a drop of 0.5 g/mL of DiI in ethanol was placed on the 22 mL coverslip and then washed off with distilled water, creating a thin layer of DiI on the coverslip surface. The DiI layer was placed on the inside of the coverslips 'sandwich', where the sample would normally be retained. Then, the coverslip was placed on the microscope stage, a drop of low-fluorescence immersion oil (Type-F, Olympus) was placed on top of the coverslip, and the quartz prism (CeNing Optics, China) was lowered onto the coverslip to generate total internal reflection. The laser was moved back and forth using the micrometer screws until an image of high fluorescence intensity was generated. Appendix A contains a more detailed alignment procedure.

3.2.6. TIRF Microscope Imaging

In the TIRF microscopy experiments, the sample between two coverslips was placed on the stage of the microscope above the objective. A drop of immersion oil was placed on the top coverslip, and the quartz prism was held in place on top of the sample to generate total internal reflection of the light from the laser. The aligned laser was run at constant power at 100 mW. All experiments occurred at room temperature (22 ± 2 °C). Appendix A contains a more detailed procedure for the experiments.

3.2.7. Capturing Images

The image size was 81.92 μm x 81.92 μm, determined from the 100x magnification, the 16 μm x 16 μm pixel size and 512 x 512 pixels of the EMCCD camera. The samples were imaged time intervals of 0.100 seconds for a total time of 10 seconds (100 frames per image). To capture the weak fluorescent signals at fast frame rates, the Horizontal Pixel Shift Readout Rate was set to 10 MHz, the Vertical Read Shift was set to 0.5 μsec, the Pre-Amplifier Gain was set to 5.1, and the EMCCD Gain was set to 300. With the Andor Solis software, each set of images was converted from a data file (SIF) into TIFF images with 8-bit black and white resolution for analysis.

3.2.8. Counting Number of Particles

The number of particles in each image was counted with Image Pro Premier (MediaCybernetics, Rockville, MD). A greyscale color threshold was manually applied to the image to identify the brighter fluorescent objects from the background. Then the computer program counted all objects that were equal or greater than 3 pixels. All objects in all of the frames for all images were counted and averaged for each set of images.

3.2.9. Measuring Two-Dimensional Diffusion

The two-dimensional diffusion of the particles was analyzed with Image Pro Premier software. For all images, a similar greyscale color threshold was manually applied to the image to identify the brighter fluorescent objects from the background. Then the "Learning" tool was applied, and a sample particle was identified through a series of images to determine the length and randomness of the particles' pathway in the image. Using the motion tracking feature, the nanoparticles were identified through a series of images using correlation tracking techniques.

With this program, nanoparticles that appeared to leave the imaging plane and then return were considered separate particles. If a nanoparticle appeared to cross paths with another, it was removed from the data. Nanoparticles that were visible for at least three consecutive images were considered for further analysis. The center of masses of all the particles and times were determined in the two-dimensional plane.

3.2.10. Analyzing Two-Dimensional Diffusion

From the center of mass data, the MSD for a particle was calculated as a function of the time interval between positions (Schmidt et al., 1995; Kummer et al., 1998):

$$MSD(\Delta t) = \frac{1}{N}\sum_{i=1}^{N}[\vec{r}(t+\Delta t) - \vec{r}(t)]^2 \tag{3.1}$$

where Δt is the time interval, N is the total number of displacements occurring during Δt, i is an individual displacement occurring during Δt (i = 1,2,3,…N), and $\vec{r}(t)$ is the position vector at time t. The MSD was ensemble averaged, and using Brownian motion models, the diffusion coefficient can be determined for two-dimensional motion with the following equation (Cussler, 2009):

$$\langle MSD(\Delta t)\rangle = 4D_{BM}\Delta t \tag{3.2}$$

where D_{BM} is the diffusion coefficient derived from Brownian motion. The diffusion coefficient was calculated for all samples weighing the errors of the MSD at each time step with the following equation:

$$D_{BM} = \frac{\sum \frac{\Delta t * \langle MSD(\Delta t) \rangle}{e_{\Delta t}^2}}{4 \sum \frac{(\Delta t)^2}{e_{\Delta t}^2}} \tag{3.3}$$

An average diffusion coefficient for each solution was determined by averaging all the diffusion coefficients for each solution. These average diffusion coefficients will be compared to the diffusion coefficient calculated with the Stokes-Einstein equation (Equation 2.6).

4. Results and Discussion

4.1 Detected Fluorescent Objects as a Function of Particle Concentration

The nanospheres were imaged at various concentrations in water to determine if the detected fluorescence is attributed to the emitted fluorescence of the fluorescent nanospheres. The images of the nanospheres at various concentrations are shown in Figures 4.1 - 4.12. The first three consecutive frames of the all samples are shown in Figures 4.1 – 4.6. It is difficult to view changes between the frames, because the brightest particles are those that are adsorbed on the surface and do not move appreciably throughout the series of images. To view diffusing molecules within the images, twelve consecutive enlarged frames are shown in Figures 4.7 – 4.12 for each concentration. It is important to note that the fluorescent objects appear to be much larger than 28 nm, due to the point spread function of the fluorescent particles. The point spread function is the three-dimensional diffraction pattern of light that is emitted from the fluorescent particle that spreads to the image plane through a high numerical aperture (NA) objective (Rottenfusser et. al, 2014).

Image Pro Premier was used to count the number of objects in each frame of images. This number was compared to the expected number of particles in each image as calculated with the following equation:

$$\#\ of\ nanospheres = \frac{6\ C\ A\ d}{\rho\ \pi\ D_{sphere}^{3}} \tag{4.1}$$

where C is the nanosphere concentration, A is the area of the image, d is the penetration depth as calculated with Equation 2.3, ρ is the density of the polystyrene spheres (Molecular Probes,

2005), and D_{sphere} is the diameter of the sphere. Table 4.1 gives the results for various concentrations of nanospheres.

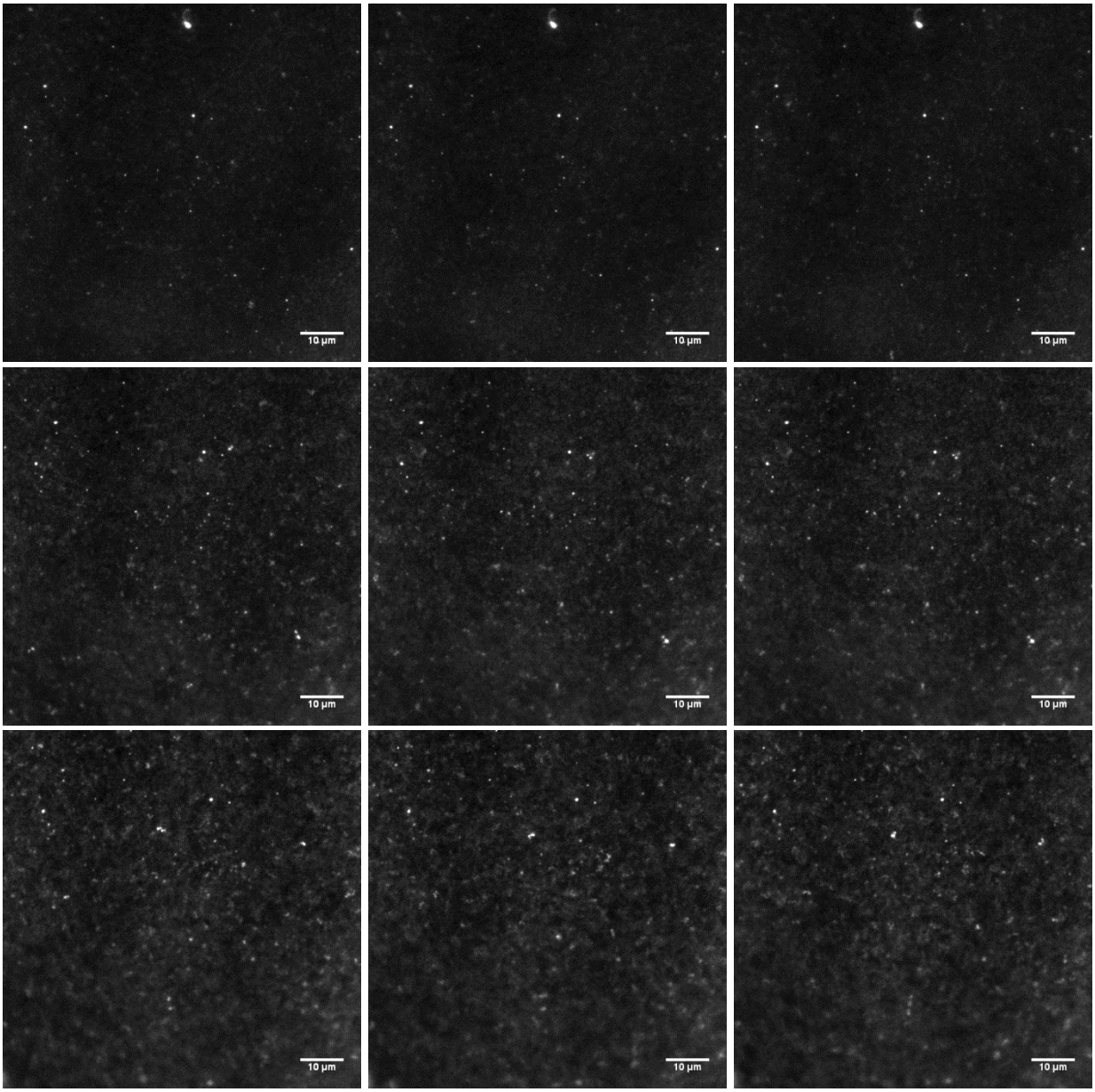

Figure 4.1. TIRF microscopy images of the nanospheres at a concentration of 2.0 x 10^{-4} g/mL. The first three consecutive frames of the three samples are shown. The scale of 10 µm is the same in all images.

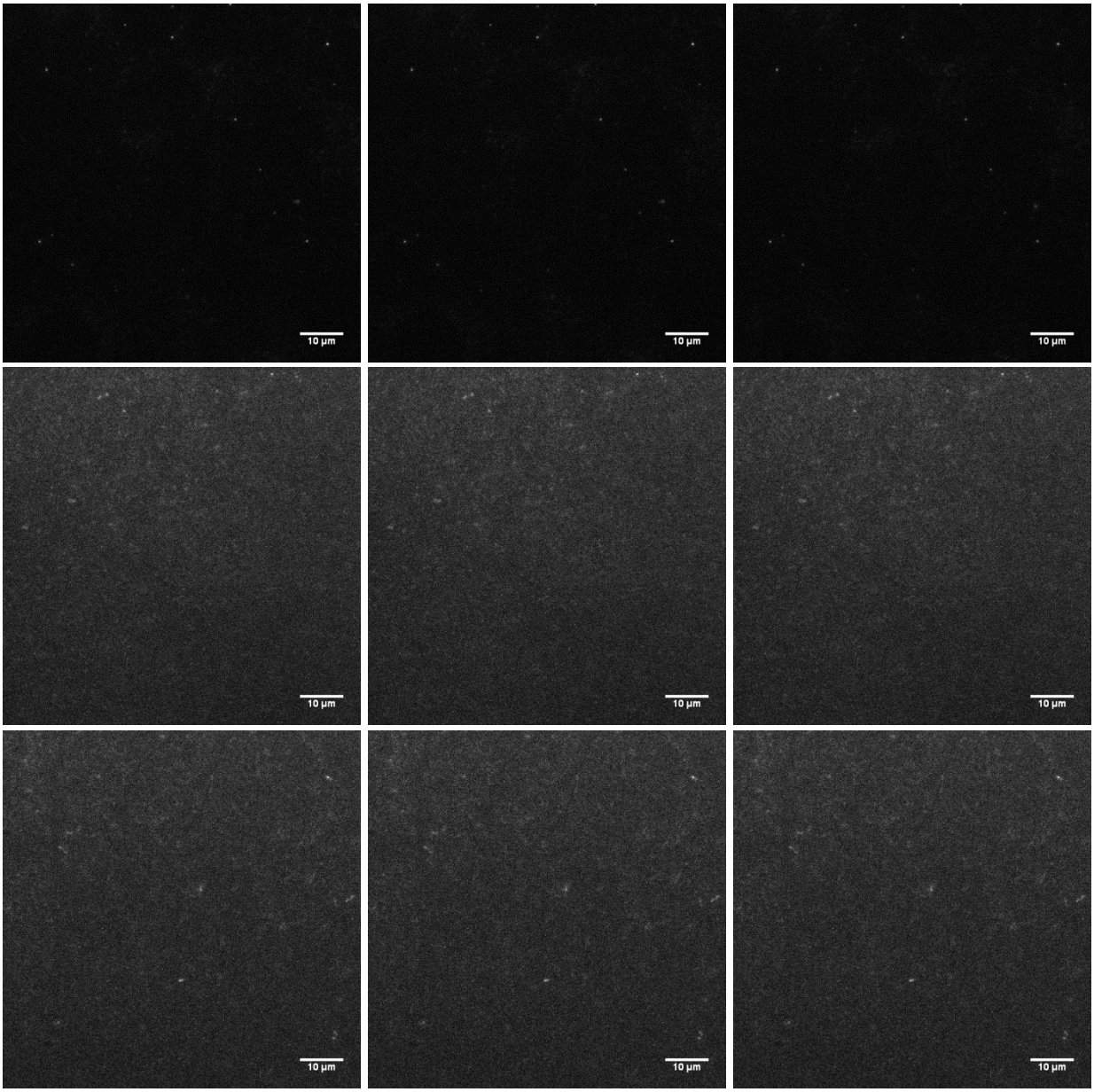

Figure 4.2. TIRF microscopy images of the nanospheres at a concentration of 4.0×10^{-5} g/mL. The first three consecutive frames of the three samples are shown. The scale of 10 µm is the same in all images.

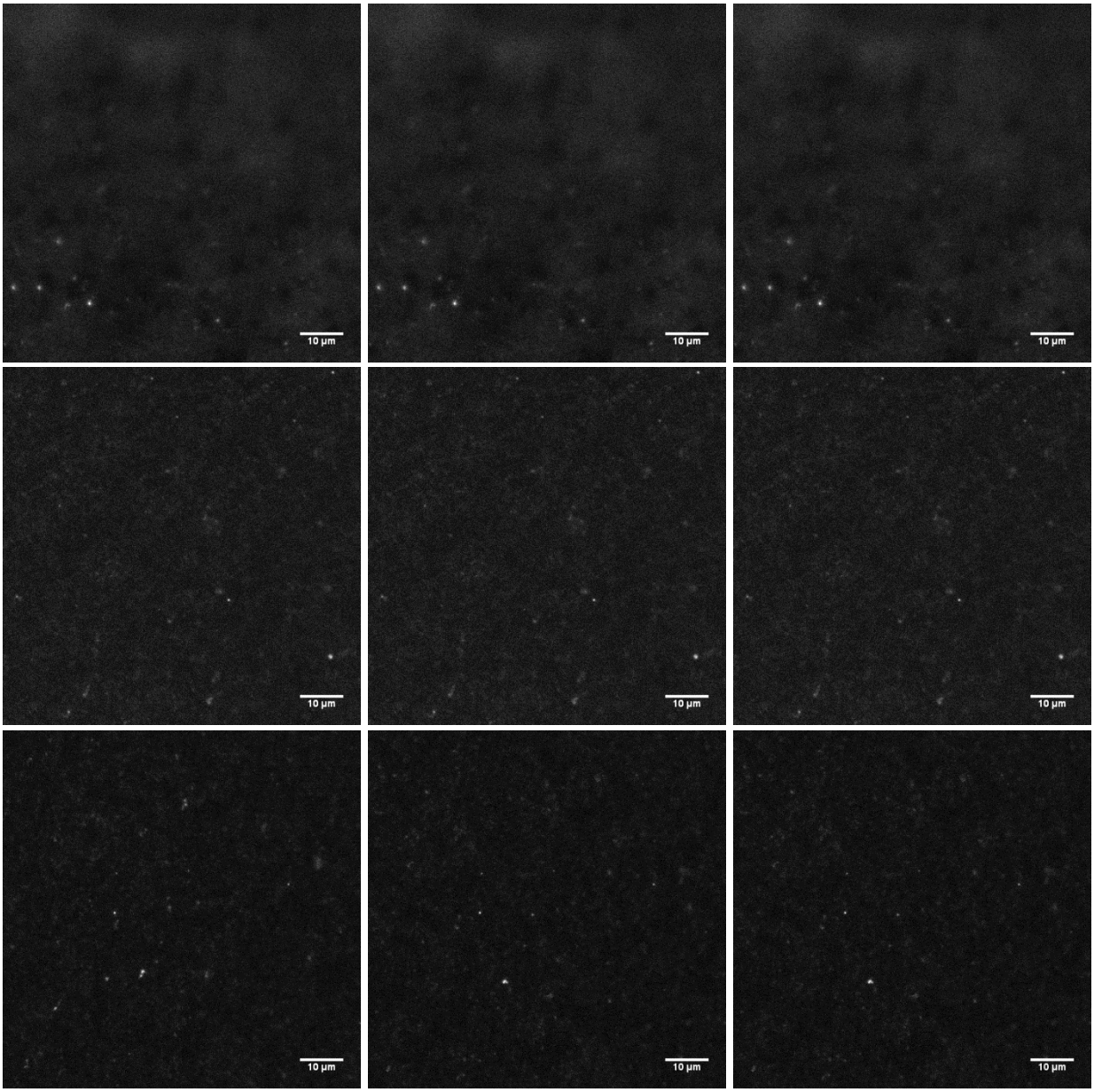

Figure 4.3. TIRF microscopy images of the nanospheres at a concentration of 2.0 x 10^{-5} g/mL. The first three consecutive frames of the three samples are shown. The scale of 10 µm is the same in all images.

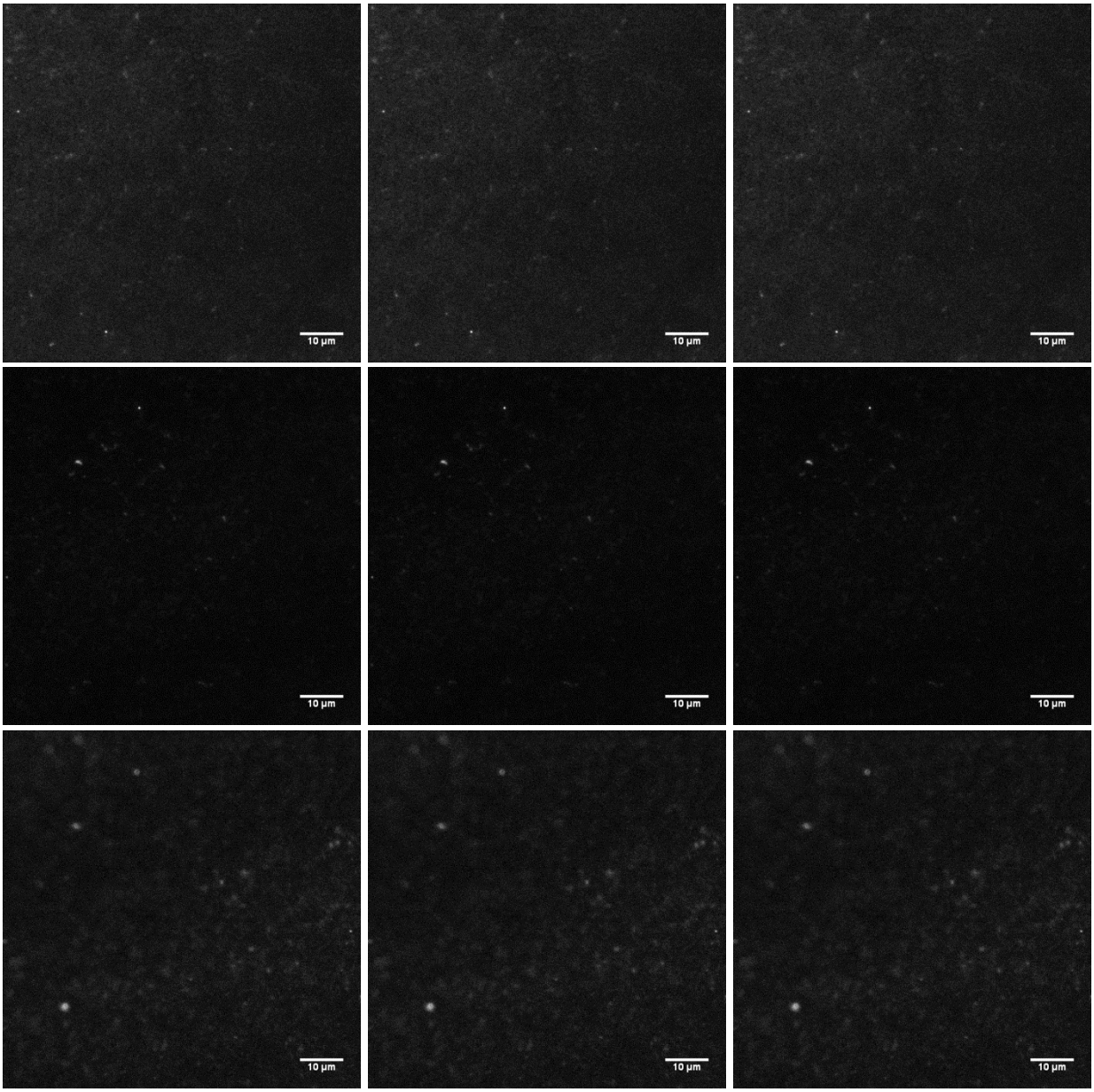

Figure 4.4. TIRF microscopy images of the nanospheres at a concentration of 1.0 x 10^{-5} g/mL. The first three consecutive frames of the three samples are shown. The scale of 10 µm is the same in all images.

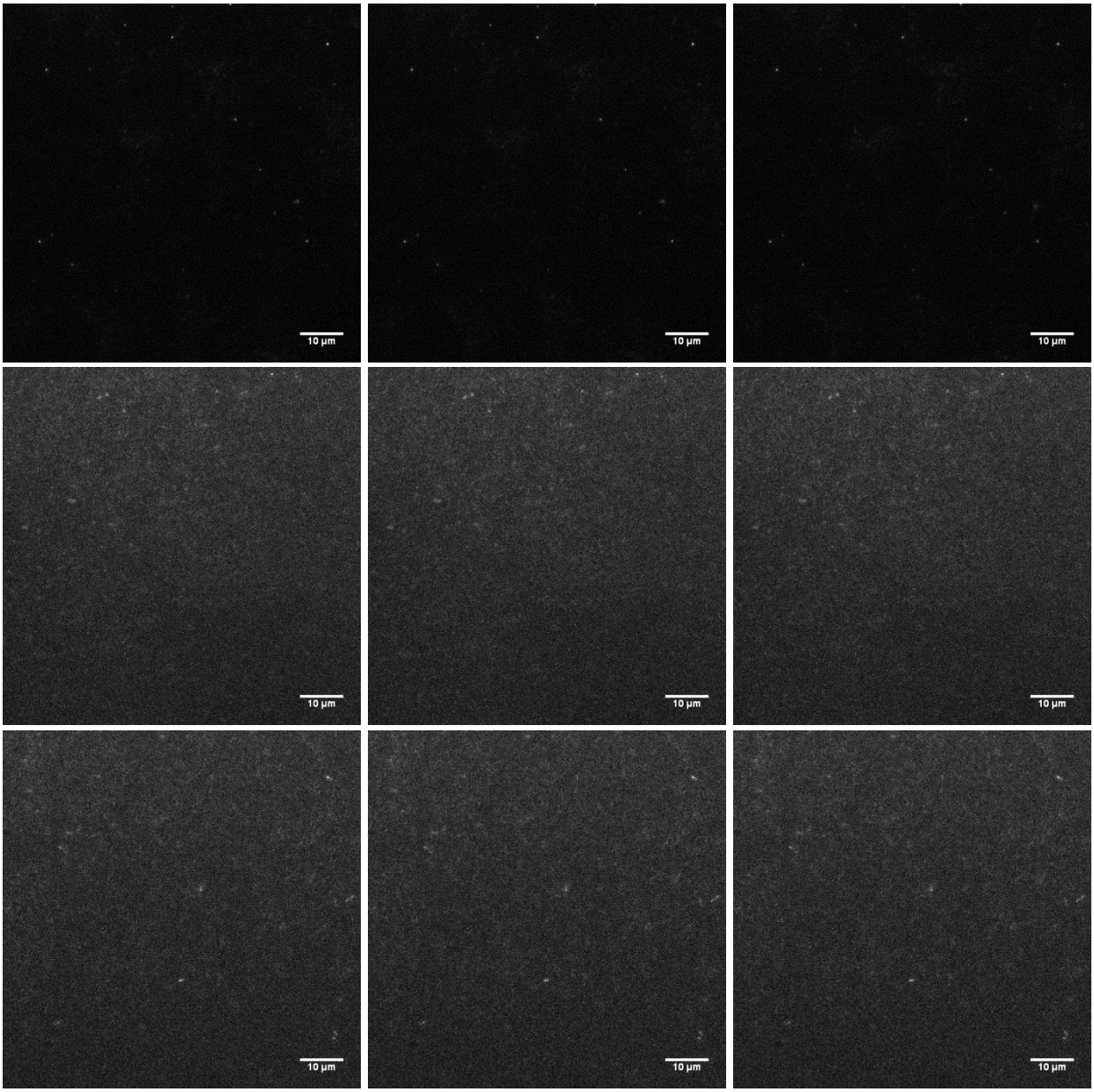

Figure 4.5. TIRF microscopy images of the nanospheres at a concentration of 4.0 x 10^{-6} g/mL. The first three consecutive frames of the three samples are shown. The scale of 10 µm is the same in all images.

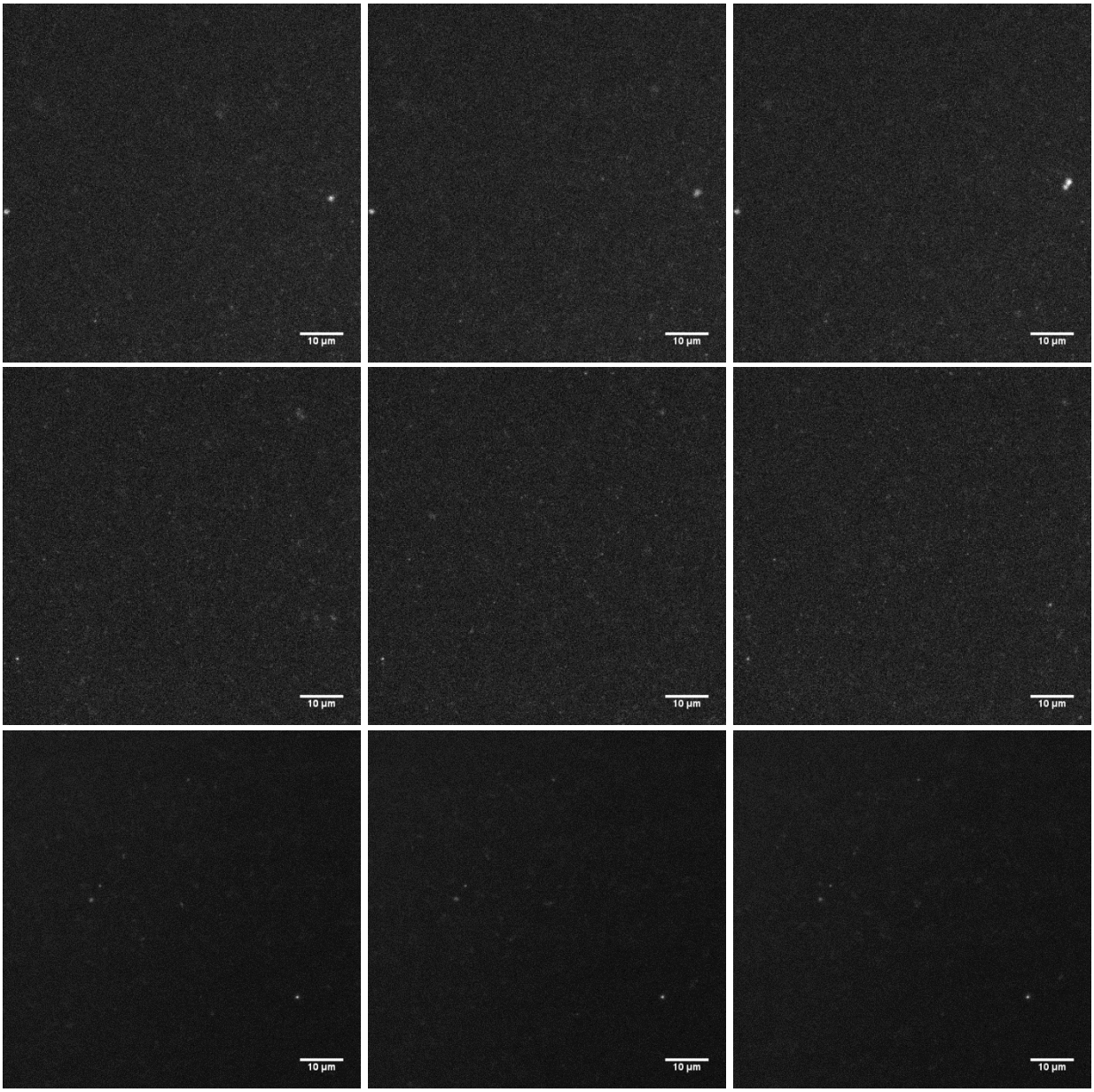

Figure 4.6. TIRF microscopy images of the nanospheres at a concentration of 2.0 x 10^{-6} g/mL. The first three consecutive frames of the three samples are shown. The scale of 10 µm is the same in all images.

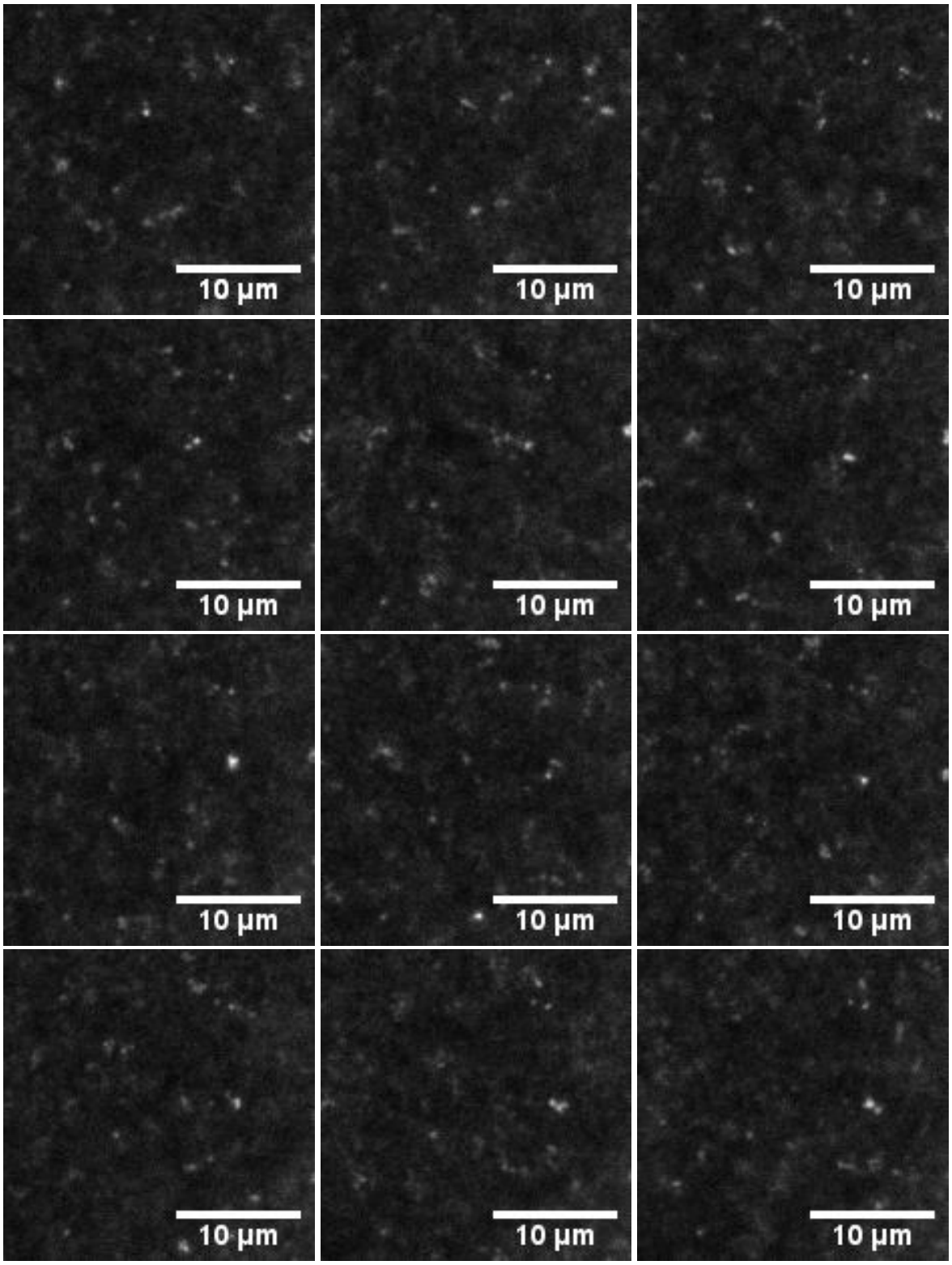

Figure 4.7. TIRF microscopy images of the nanospheres at a concentration of 2.0 x 10^{-4} g/mL. Twelve consecutive image frames are shown from Sample 2. The scale of 10 µm is the same in all images.

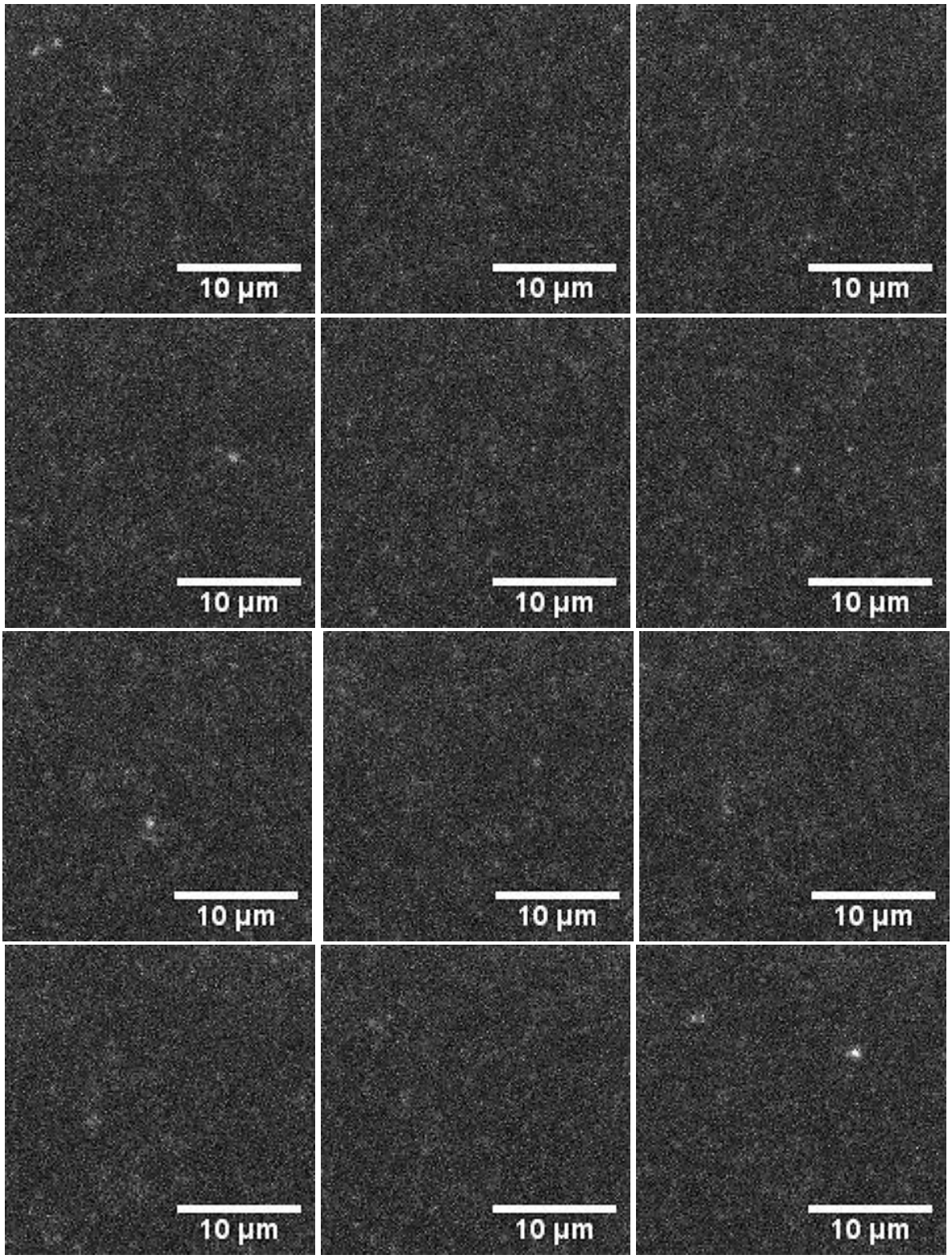

Figure 4.8. Enhanced TIRF microscopy images of the nanospheres at a concentration of 4.0 x 10^{-5} g/mL. Twelve consecutive image frames are shown from Sample 2. The scale of 10 µm is the same in all images.

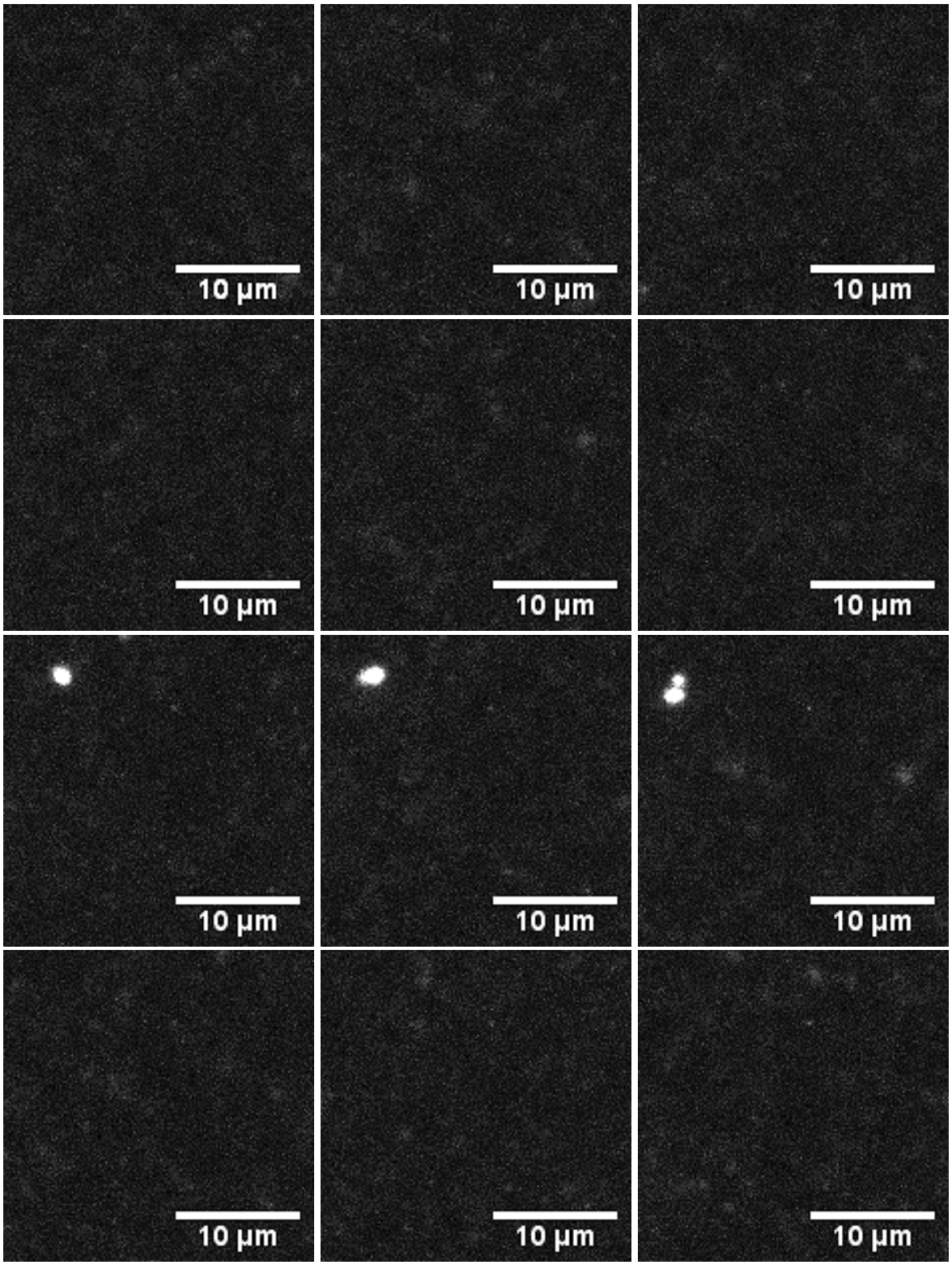

Figure 4.9. Enhanced TIRF microscopy images of the nanospheres at a concentration of 2.0×10^{-5} g/mL. Twelve consecutive image frames are shown from Sample 2. The scale of 10 µm is the same in all images.

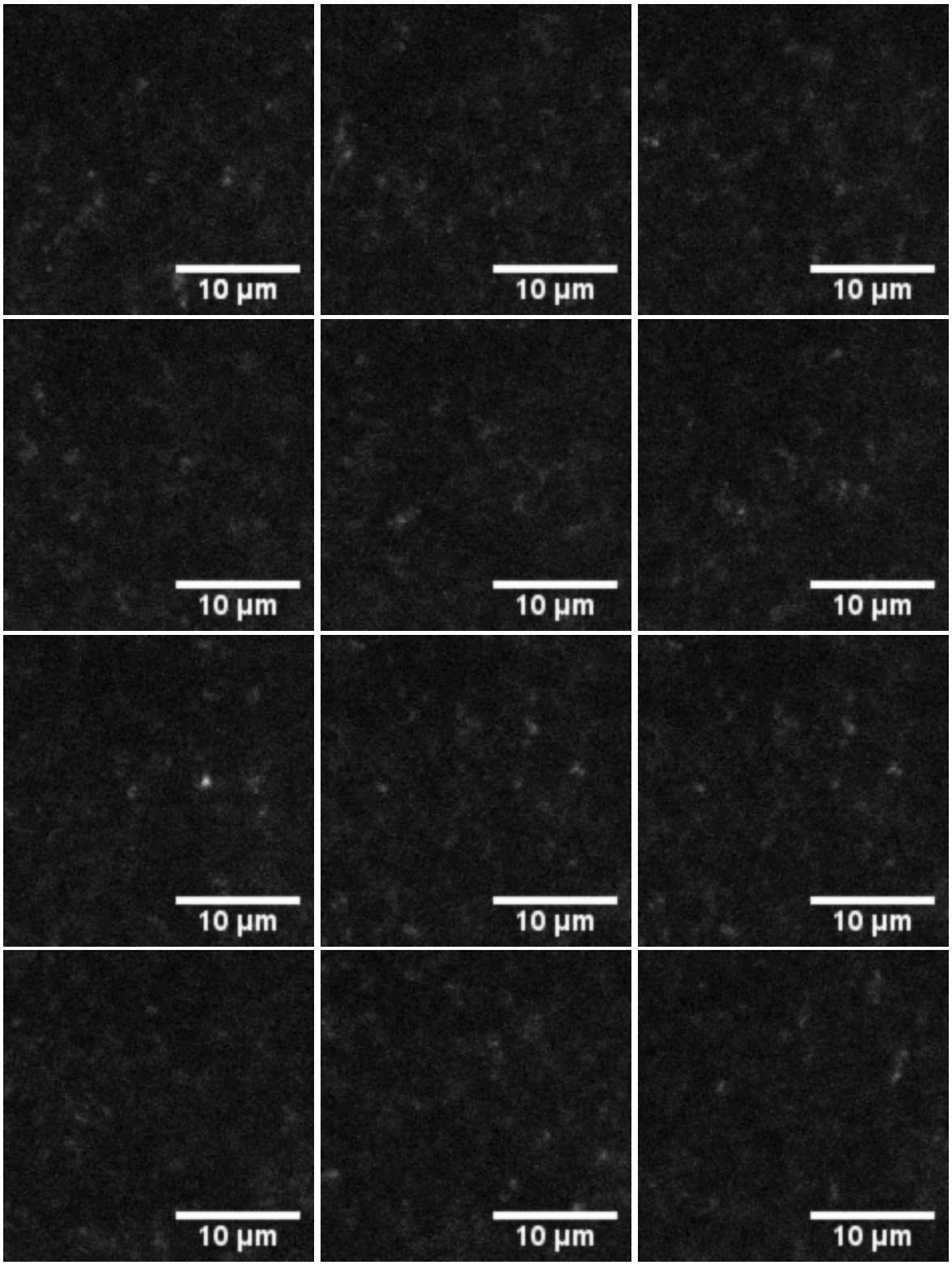

Figure 4.10. Enhanced TIRF microscopy images of the nanospheres at a concentration of 1.0 x 10^{-5} g/mL. Twelve consecutive image frames are shown from Sample 3. The scale of 10 µm is the same in all images.

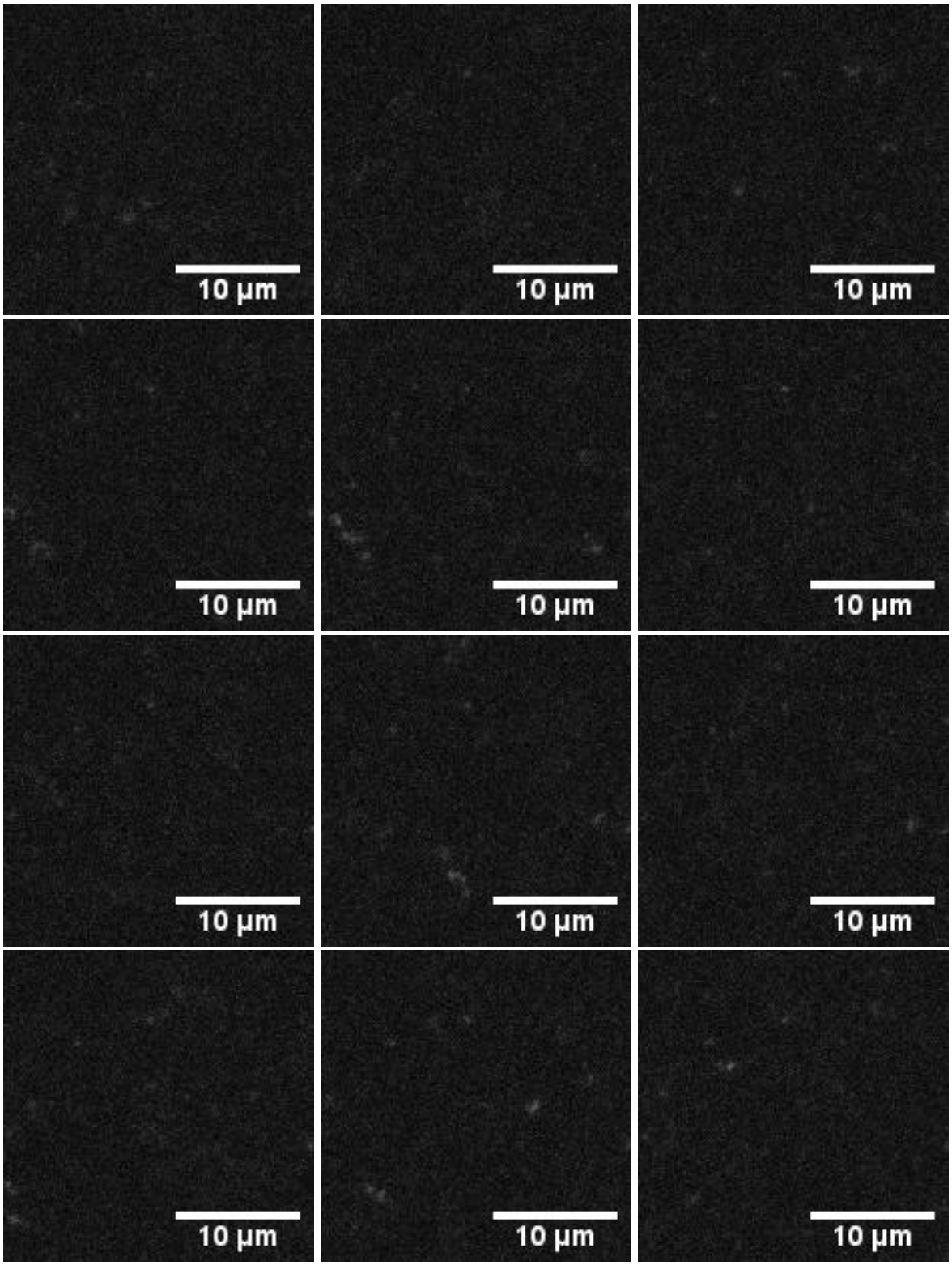

Figure 4.11. Enhanced TIRF microscopy images of the nanospheres at a concentration of 4.0 x 10^{-6} g/mL. Twelve consecutive image frames are shown from Sample 2. The scale of 10 µm is the same in all images.

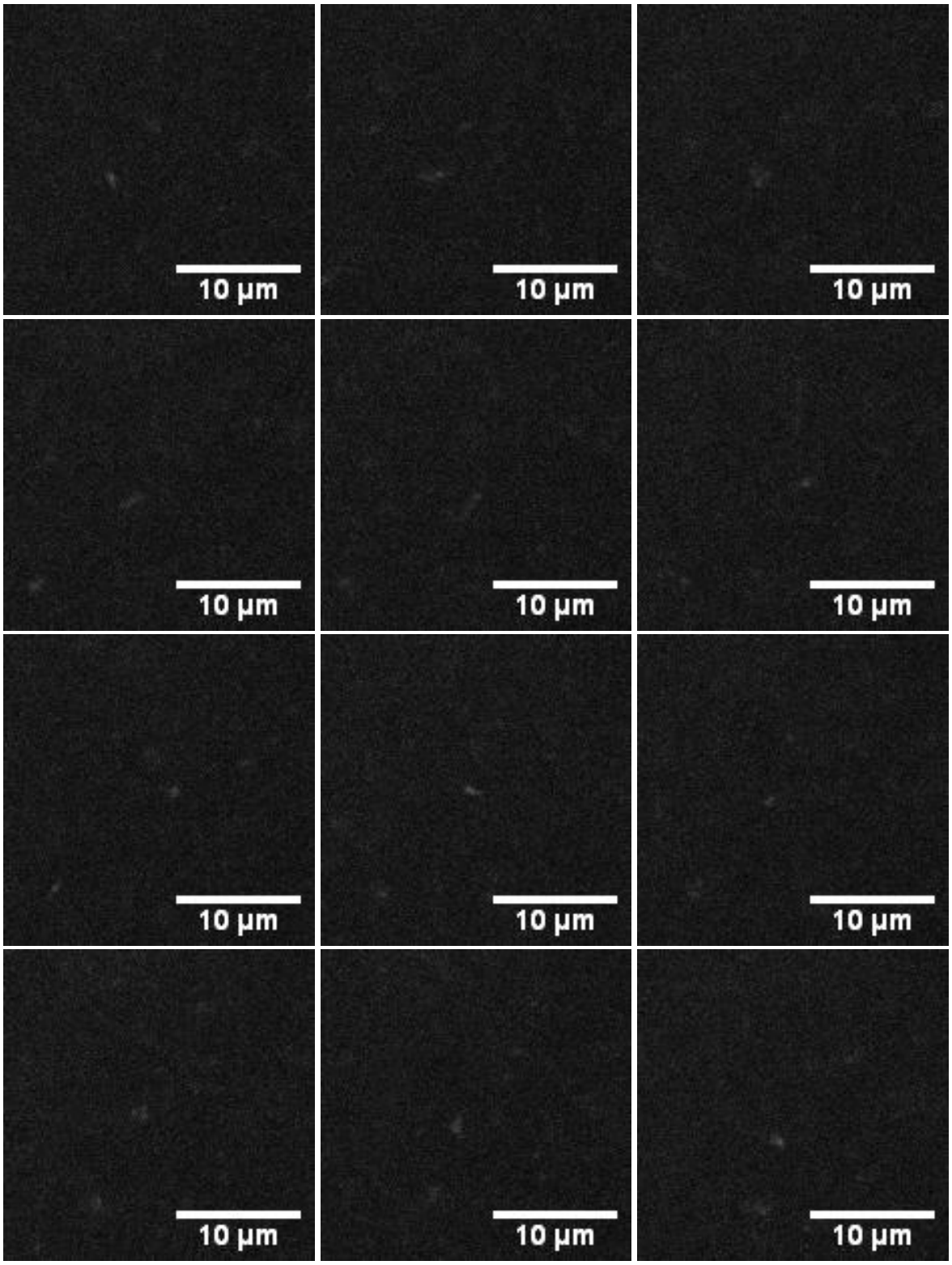

Figure 4.12. Enhanced TIRF microscopy images of the nanospheres at a concentration of 2.0×10^{-6} g/mL. Twelve consecutive image frames are shown from Sample 2. The scale of 10 µm is the same in all images.

Table 4.1. Number of objects detected as a function of nanosphere concentration.

Concentration (g/mL)	2.0×10^{-4}	4.0×10^{-5}	2.0×10^{-5}	1.0×10^{-5}	4.0×10^{-6}	2.0×10^{-6}
Percent diluted		20%	10%	5%	2%	1%
Expected number of nanospheres in all frames in each image	14000	2800	1400	700	280	140
Average number of objects detected in all frames of each image	220 +/- 110	42 +/- 14	21 +/- 5	11 +/- 3	8 +/- 1	6 +/- 1
Percent of maximum detected objects		19%	9%	5%	4%	3%

As the nanosphere concentration decreased, the number of detected fluorescent nanospheres objects decreased in proportion to the nanosphere concentration, so the fluorescence observed was due to the fluorescent nanospheres. However, the number of nanospheres in the images was approximately smaller by $1/64^{th}$ of the number of nanospheres calculated with Equation 4.1. There are two possible reasons for this large discrepancy. Fluorescence in the evanescent wave is very low, so particles away from the refractive interface may not be visible. Also, there could be repulsive interactions between the glass, which is negatively charged, and the nanospheres, which are also negatively charged that might keep the nanospheres concentration low near the refractive interface.

The microscope setup might offer a low fluorescence collection efficiency, which could yield a lower than expected amount of fluorescent objects in the images. The collection efficiency of the objective lens does decrease as the distance from the prism-coverslip interface increases due to the exponential decay of the evanescent wave, so it is possible that less diffusing objects are detected during the experiments (Mattheyses and Axelrod, 2006). The fluorescence collection efficiency for this system is defined in this case as the percentage of emitted light that

is collected by the CCD camera. This can be estimated based on the transmittance efficiencies of the objective lens and barrier filter and the quantum efficiency of the EMCCD camera. Based on the information provided by the Olympus, Chroma Technology, and Andor, the collection efficiency would be approximately 83%, so the microscopy system is not the primary cause of the difference between observed and estimated number of nanoparticles.

4.2 Diffusion Coefficient Measurement as a Function of Solution Viscosity

The fluorescent nanoparticles at a concentration of 2.0 x 10^{-6} g/mL were imaged in triplicate in three different solutions: distilled water, 20 vol. % glycerol, and 40 vol. % glycerol. The nanoparticles appeared to diffuse randomly in a two-dimensional motion. From successive images, the two-dimensional trajectories were tracked. Figures 4.13-4.15 show the two-dimensional trajectories of a nanoparticle in each of the three solutions.

The mean squared displacement was calculated from the two-dimensional trajectories using Equation 3.3. The diffusion coefficient was then determined from the slope of a plot of MSD vs. time interval. Figures 4.16-4.24 show the average MSD of all the particles vs. time interval in each solution. The MSD vs. time interval plot is fairly linear, as the average correlation coefficient value was 0.87, suggesting that the mechanism for diffusion was by Brownian motion (Cussler, 2009; Vrljic, 2007). The relationship between MSD and viscosity also followed the Stokes-Einstein theory, for which the diffusion coefficient is inversely proportional to the viscosity of the solution.

The diffusion coefficients of all the samples were averaged for each solution, and the results are summarized in Table 4.2 and compared with the diffusion coefficients calculated by the Stokes-Einstein equation. The standard deviation of the calculated average diffusion coefficient is the standard deviation of the three samples.

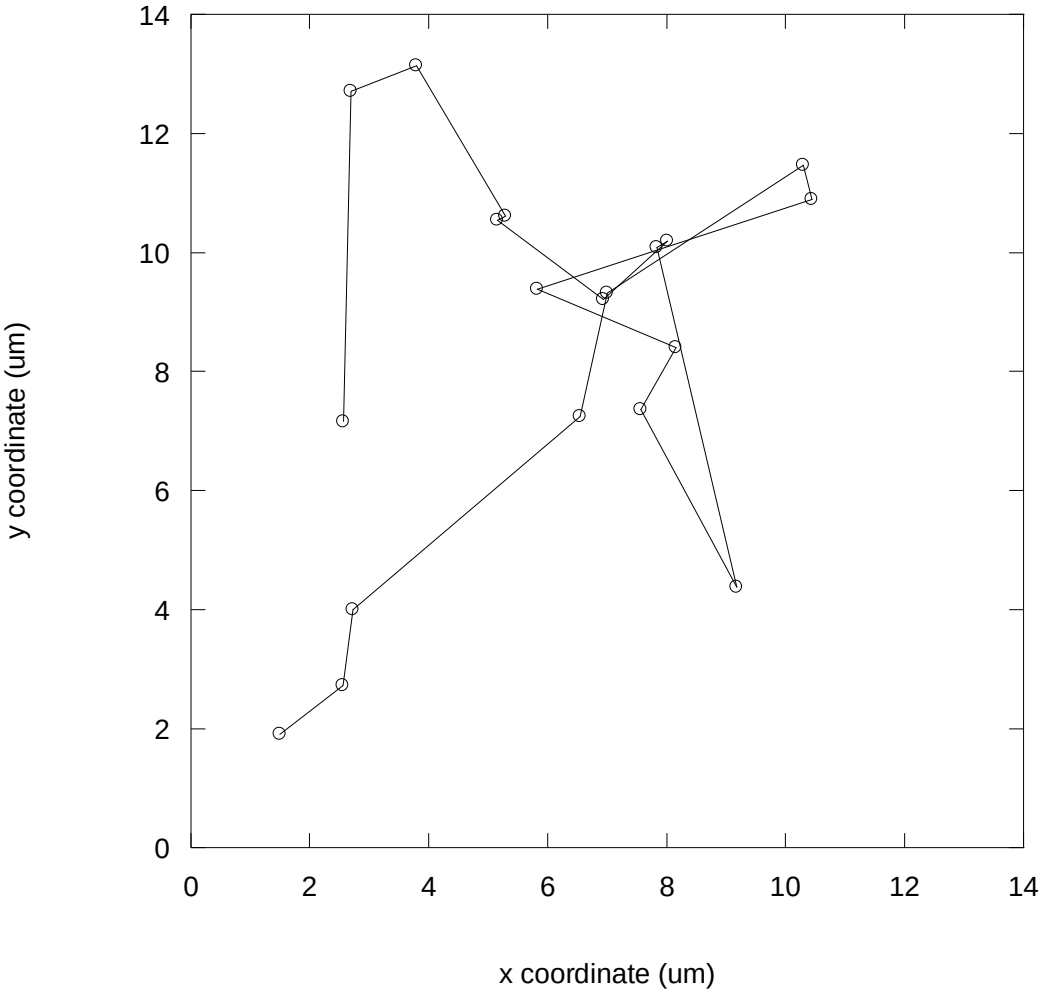

Figure 4.13. The entire two-dimensional trajectory of a nanoparticle in water. Each data point represents the center of mass at time intervals of 0.100 s.

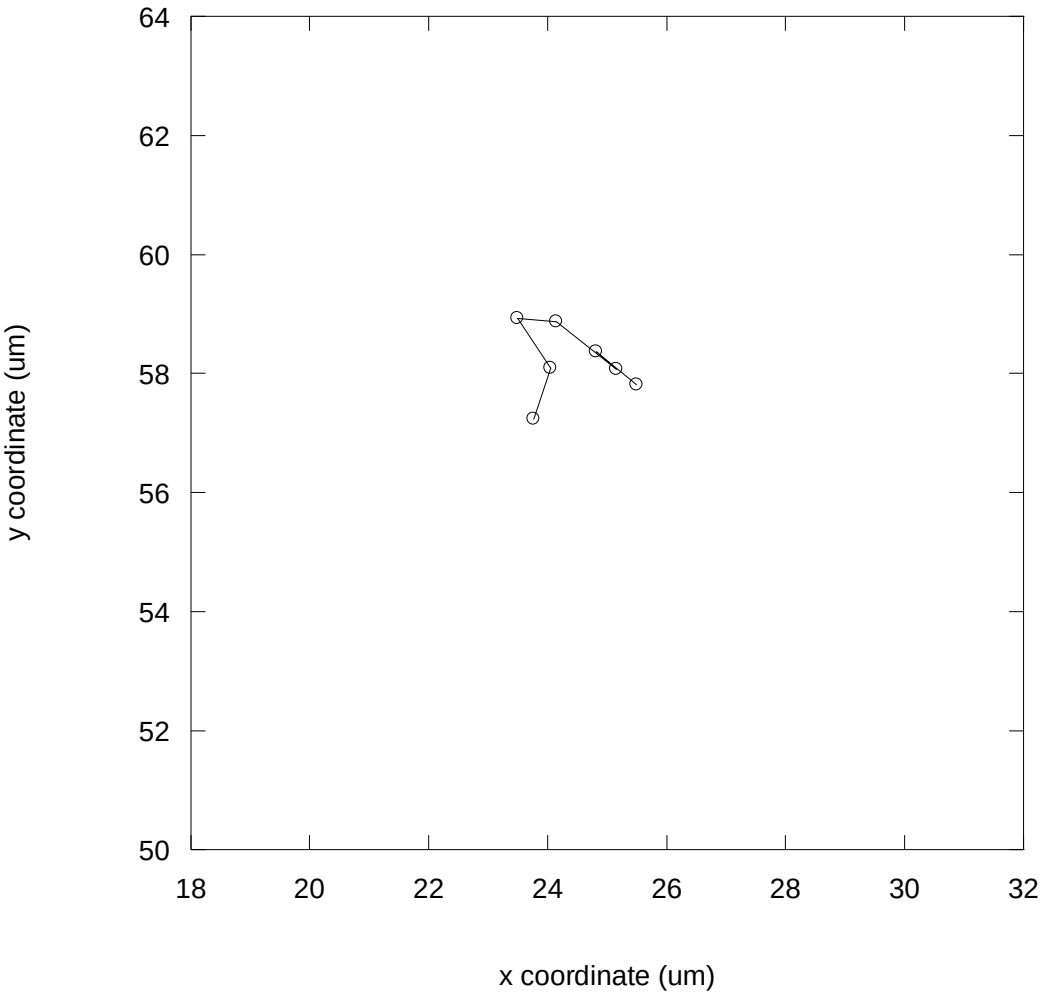

Figure 4.14. The entire two-dimensional trajectory of a nanoparticle in 20% vol. glycerol. Each data point represents the center of mass at time intervals of 0.100 s.

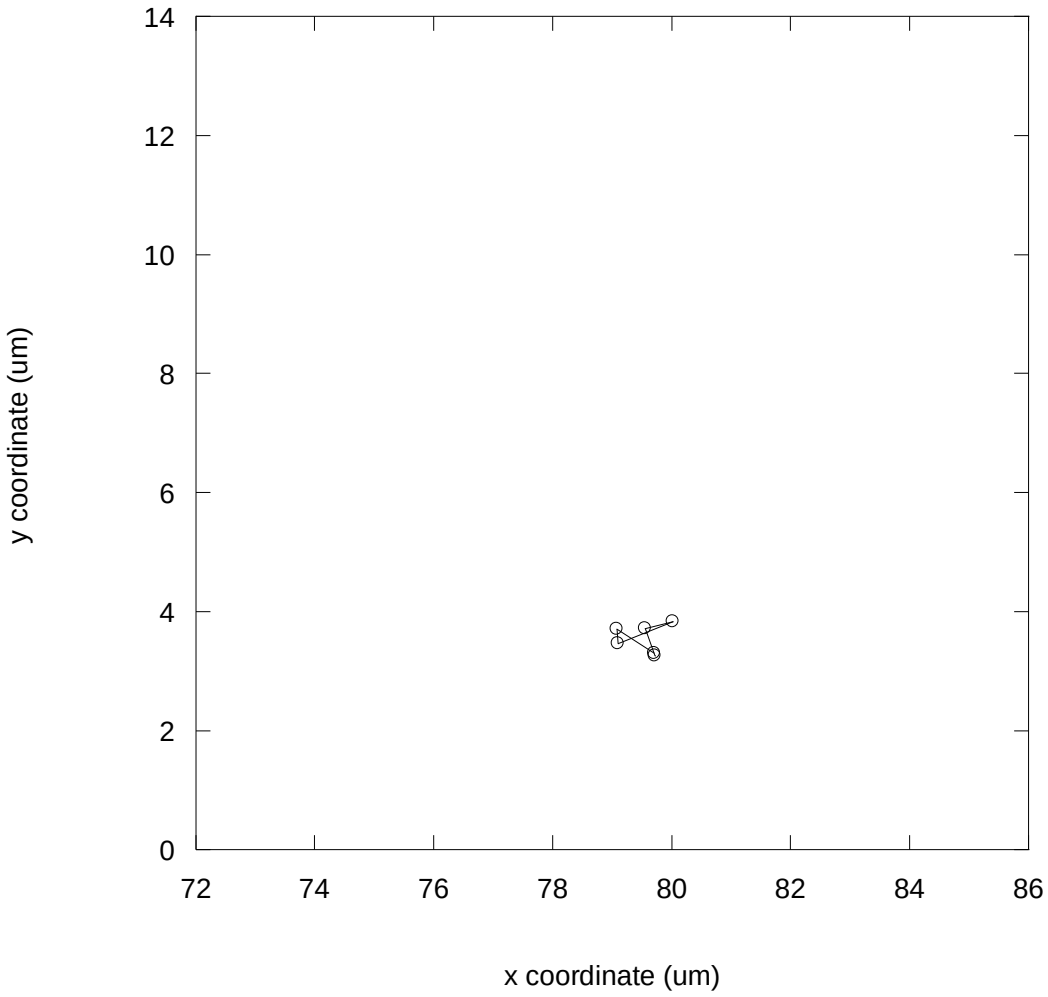

Figure 4.15. The entire two-dimensional trajectory of a nanoparticle in 40% vol. glycerol. Each data point represents the center of mass at time intervals of 0.100 s.

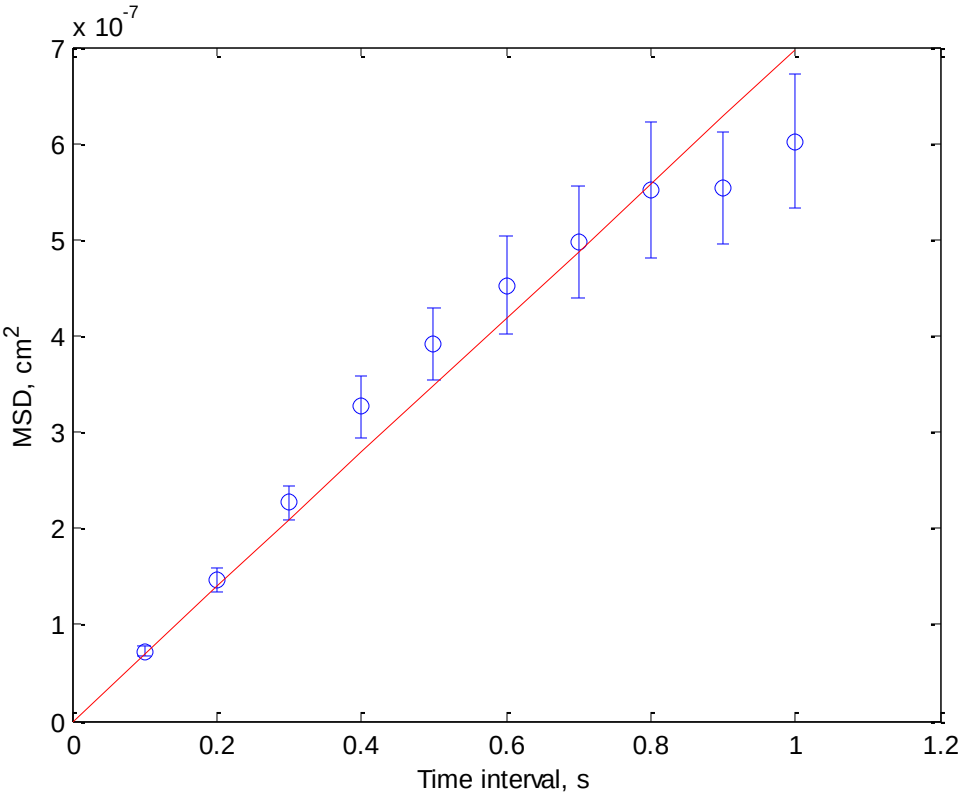

Figure 4.16. Ensemble-averaged MSD vs. time interval for sample 1 of the solution of 2.0 x 10^{-6} g/mL nanoparticles in water. The number of nanospheres averaged for each data point are 193, 193, 162, 132, 112, 93, 82, 74, 68, and 66. The error bars represent the standard error. The solid line is a fit of Equation 3.3 to the data (r^2 = 0.93). From the slope of this linear fit, the diffusion coefficient is equal to 1.7 ± 0.6 x 10^{-7} cm^2/s.

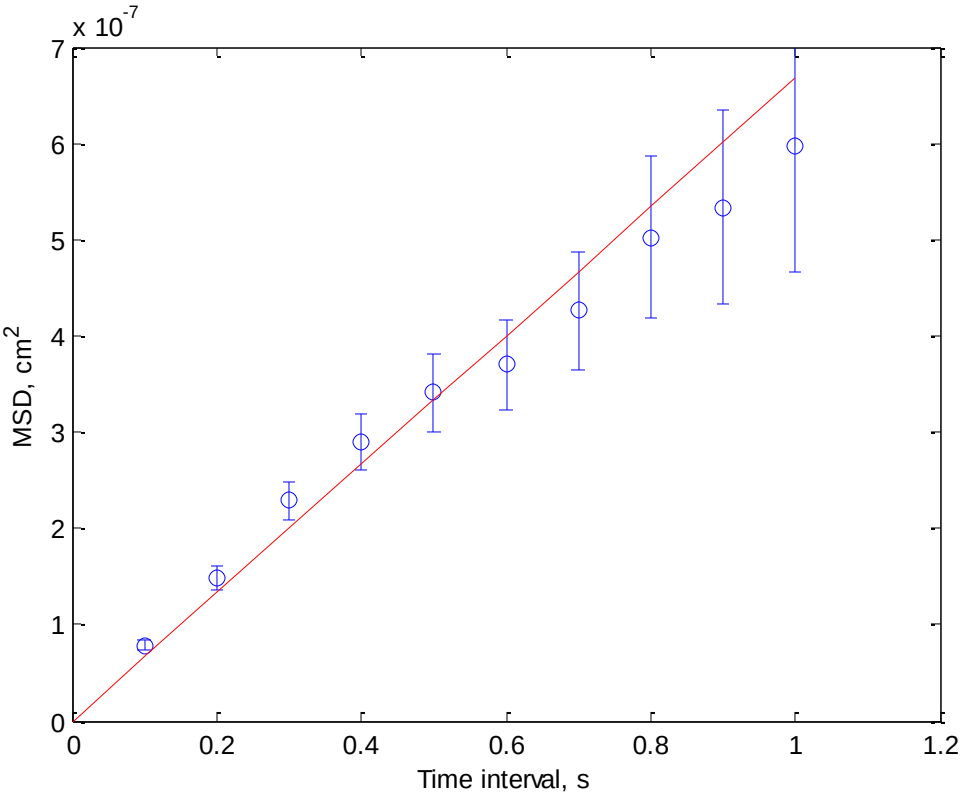

Figure 4.17. Ensemble-averaged MSD vs. time interval for sample 2 of the solution of 2.0 x 10^{-6} g/mL nanoparticles in water. The number of nanospheres averaged for each data point are 202, 202, 159, 115, 92, 72, 61, 54, 43, and 37. The error bars represent the standard error. The solid line is a fit of Equation 3.3 to the data (r^2 = 0.94). From the slope of this linear fit, the diffusion coefficient is equal to 1.7 ± 0.6 x 10^{-7} cm^2/s.

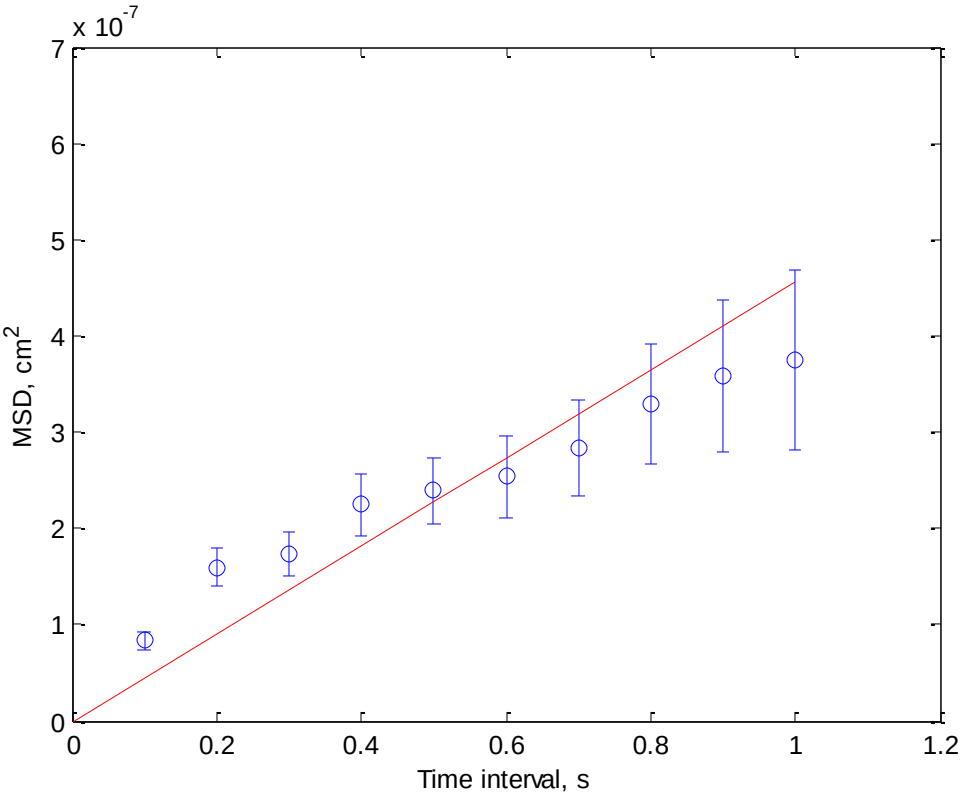

Figure 4.18. Ensemble-averaged MSD vs. time interval for sample 3 of the solution of 2.0 x 10^{-6} g/mL nanoparticles in water. The number of nanospheres averaged for each data point are 81, 81, 61, 46, 40, 35, 29, 25, 19, and 19. The error bars represent the standard error. The solid line is a fit of Equation 3.3 to the data (r^2 = 0.72). From the slope of this linear fit, the diffusion coefficient is equal to 1.1 ± 0.4 x 10^{-7} cm^2/s.

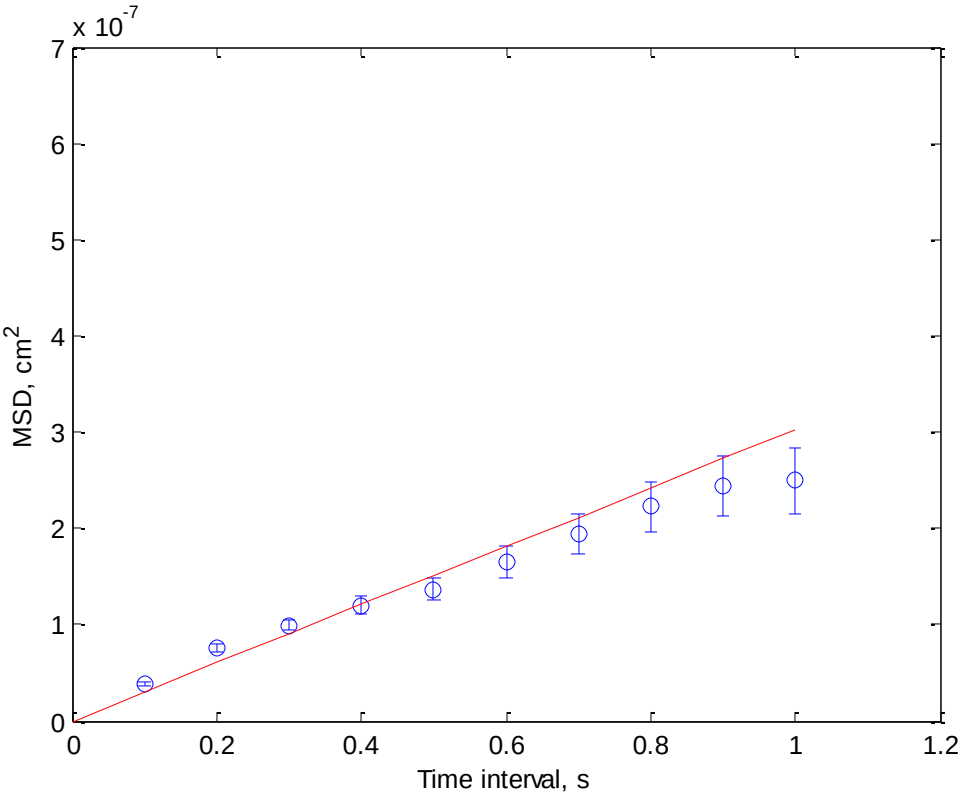

Figure 4.19. Ensemble-averaged MSD vs. time interval for sample 1 of the solution of 2.0 x 10^{-6} g/mL nanoparticles in 20% vol. glycerol. The number of nanospheres averaged for each data point are 355, 355, 287, 221, 192, 164, 146, 135, 118, and 111. The error bars represent the standard error. The solid line is a fit of Equation 3.3 to the data (r^2 = 0.89). From the slope of this linear fit, the diffusion coefficient is equal to 7.6 ± 2.8 x 10^{-8} cm^2/s.

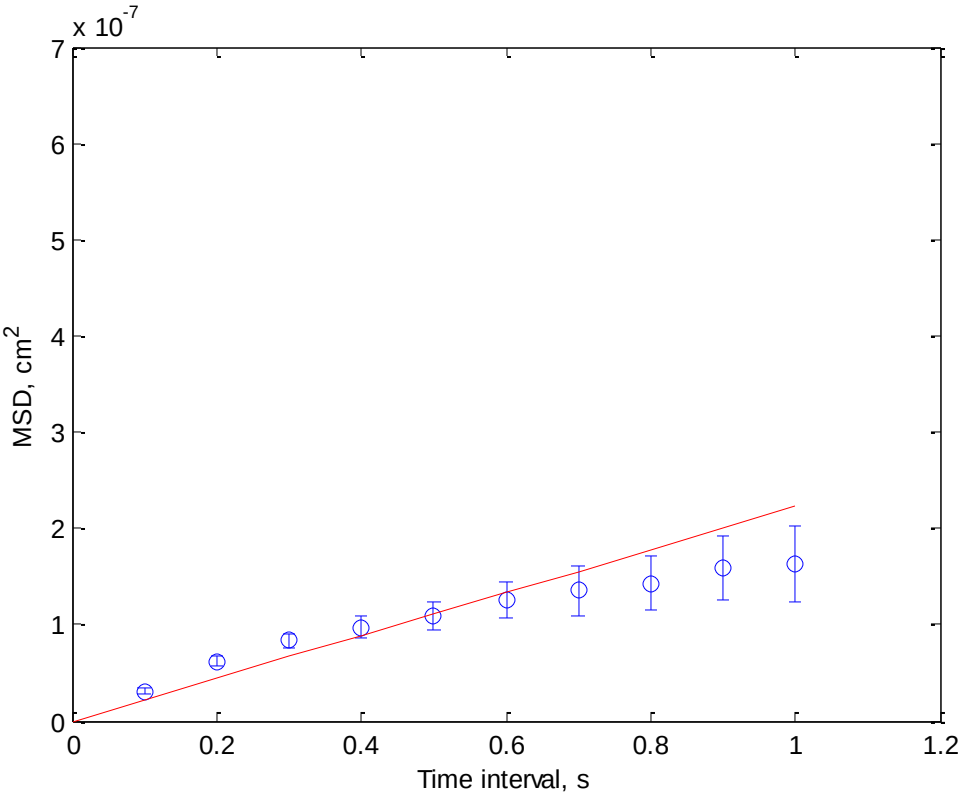

Figure 4.20. Ensemble-averaged MSD vs. time interval for sample 2 of the solution of 2.0 x 10^{-6} g/mL nanoparticles in 20% vol. glycerol. The number of nanospheres averaged for each data point are 218, 218, 169, 135, 112, 96, 84, 74, 69, and 65. The error bars represent the standard error. The solid line is a fit of Equation 3.3 to the data (r^2 = 0.54). From the slope of this linear fit, the diffusion coefficient is equal to 5.6 ± 2.6 x 10^{-8} cm^2/s.

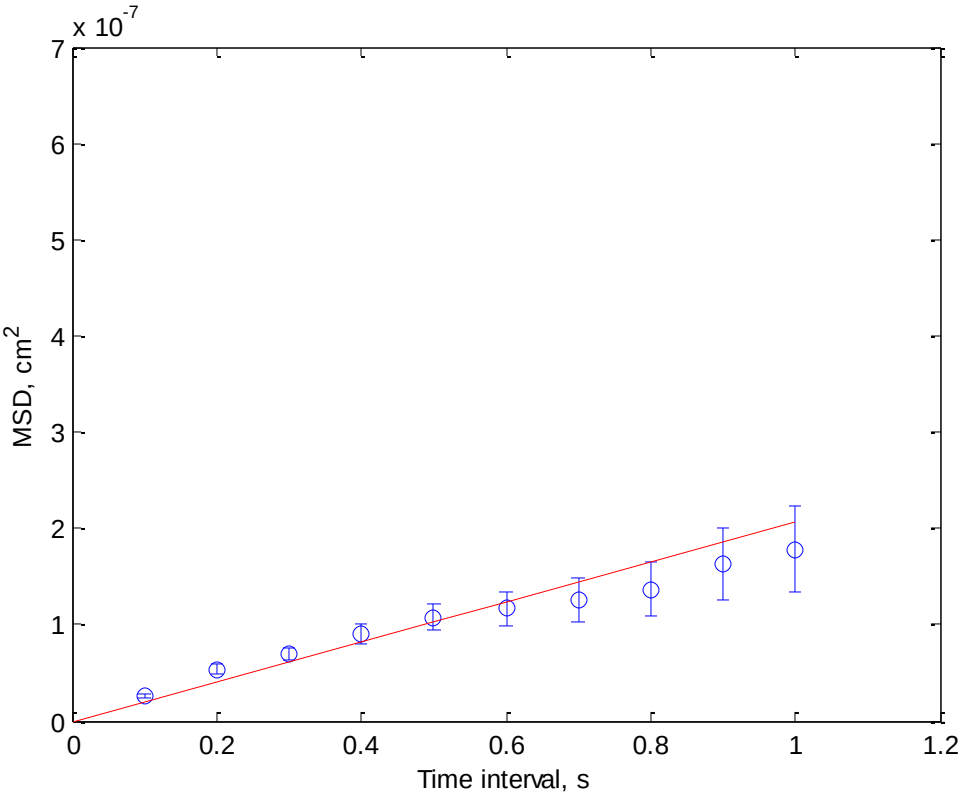

Figure 4.21. Ensemble-averaged MSD vs. time interval for sample 3 of the solution of 2.0 x 10^{-6} g/mL nanoparticles in 20% vol. glycerol. The number of nanospheres averaged for each data point are 213, 213, 170, 134, 115, 93, 74, 60, 50, and 48. The error bars represent the standard error. The solid line is a fit of Equation 3.3 to the data (r^2 = 0.85). From the slope of this linear fit, the diffusion coefficient is equal to 5.2 ± 2.4 x 10^{-8} cm^2/s.

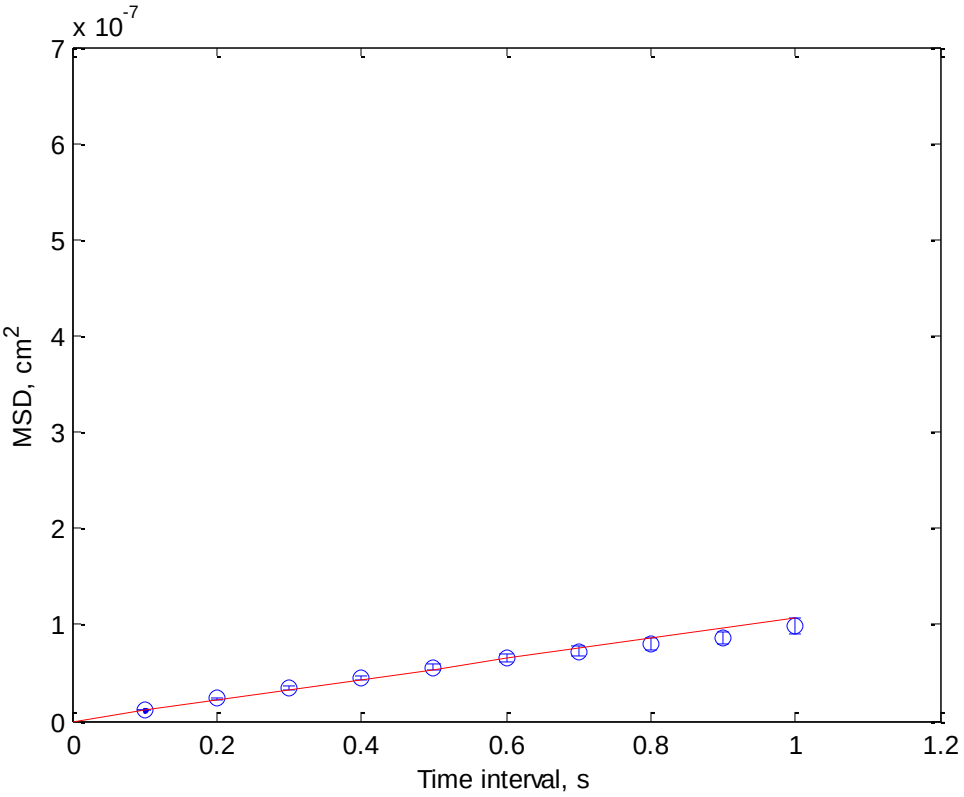

Figure 4.22. Ensemble-averaged MSD vs. time interval for sample 1 of the solution of 2.0 x 10^{-6} g/mL nanoparticles in 40% vol. glycerol. The number of nanospheres averaged for each data point are 667, 667, 519, 398, 302, 249, 206, 182, 152, and 135. The error bars represent the standard error. The solid line is a fit of Equation 3.3 to the data (r^2 = 0.97). From the slope of this linear fit, the diffusion coefficient is equal to 2.7 ± 0.8 x 10^{-8} cm^2/s.

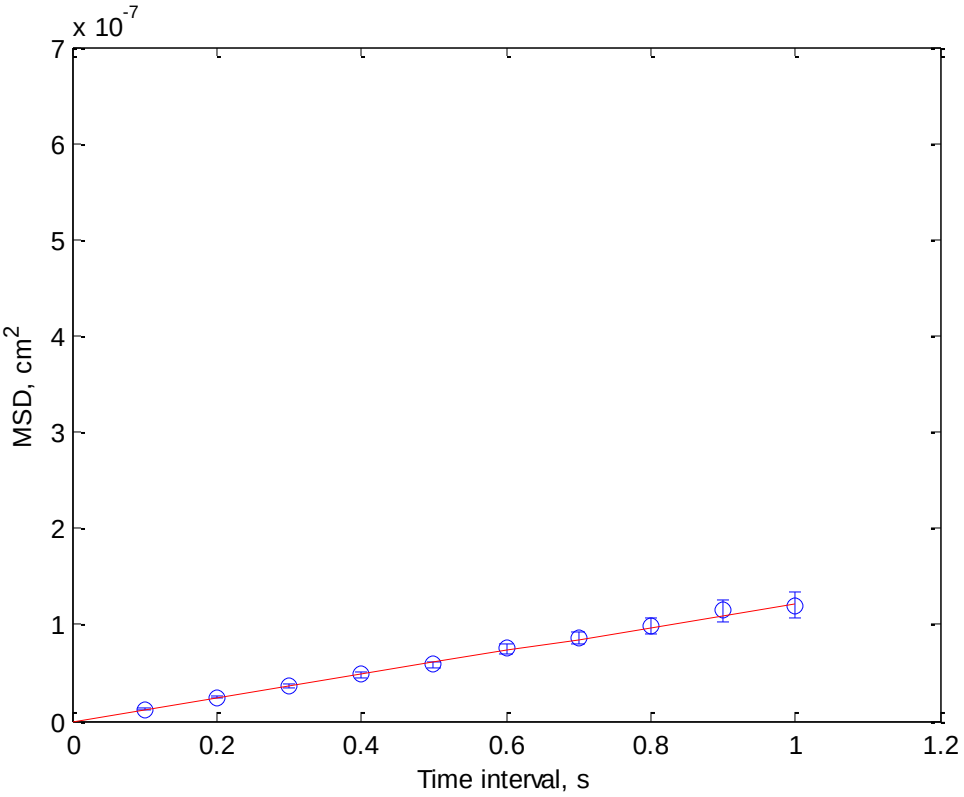

Figure 4.23. Ensemble-averaged MSD vs. time interval for sample 2 of the solution of 2.0 x 10^{-6} g/mL nanoparticles in 40% vol. glycerol. The number of nanospheres averaged for each data point are 436, 436, 342, 247, 192, 157, 129, 107, 97, and 83. The error bars represent the standard error. The solid line is a fit of Equation 3.3 to the data (r^2 = 0.99). From the slope of this linear fit, the diffusion coefficient is equal to 3.0 ± 0.8 x 10^{-8} cm^2/s.

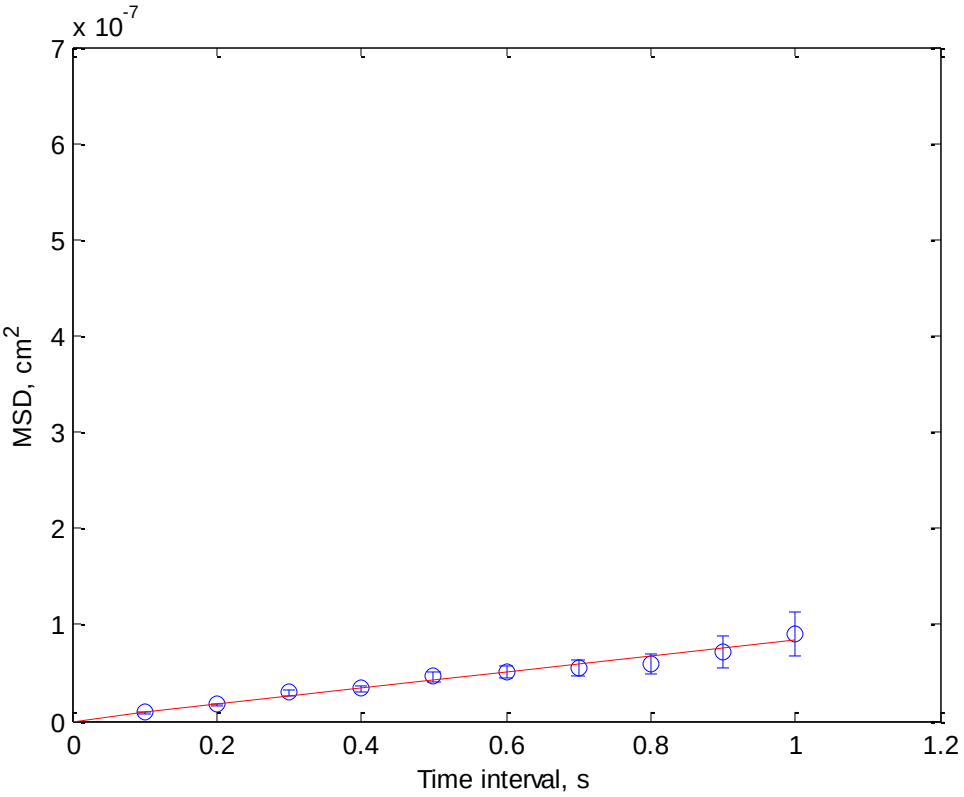

Figure 4.24. Ensemble-averaged MSD vs. time interval for sample 3 of the solution of 2.0 x 10^{-6} g/mL nanoparticles in 40% vol. glycerol. The number of nanospheres averaged for each data point are 359, 359, 260, 196, 165, 133, 107, 92, 77, and 59. The error bars represent the standard error. The solid line is a fit of Equation 3.3 to the data (r^2 = 0.96). From the slope of this linear fit, the diffusion coefficient is equal to 2.1 ± 0.7 x 10^{-8} cm^2/s.

Table 4.2. Measured average and theoretical diffusion coefficient for each solution.

Solution	**Viscosity at 22°C (cP)***	**Diffusion Coefficient from Single Particle Tracking (x 10^{-7} cm^2/s)**	**Diffusion Coefficient from Stokes-Einstein (x 10^{-7} cm^2/s)**
Water	0.957	1.5 ± 0.5	1.6
20% vol Glycerol	1.88	0.61 ± 0.26	0.83
40% vol Glycerol	4.50	0.26 ± 0.08	0.35

* Viscosity values from Cheng, 2008.

Experimental and estimated diffusion coefficients have the same magnitude and decrease similarly in the more viscous glycerol solutions. For the water/glycerol solutions, the agreement is actually better. As seen in Figures 4.16, 4.17, and 4.18, the linearity of the MSD vs. time interval in 40% vol. glycerol is actually much better than those in water and 20 % vol. glycerol (Figures 4.10-4.15). There are more observed nanoparticles in the images of the glycerol solutions due to an increase in solvent viscosity as more particles remain in consecutive frames for a greater length of time in more viscous solutions. Interestingly, the number of trajectories does not increase linearly with penetration depth of the image. This could be due to the fact that the nanoparticles tend to remain in the evanescent wave for longer periods of time.

All of the experimental diffusion coefficients were less than the theoretical values, which can be attributed to adsorption of the nanoparticles to the coverslip. Some adsorption was evident in all of the images, but there seemed to be less adsorption as the glycerol concentration in the solution increased. The adsorption was also evident in Figures 4.10-4.15 as the experimental MSD values are less than the linear trend at times greater than 0.8 s. Nanoparticle trajectories that showed adsorption were manually removed, however it is rather impossible to remove all trajectories, especially those where adsorption occurs over short time intervals. This proves that it will be necessary for future studies to determine a method to remove adsorption.

5. Conclusions

A TIRF microscopy system has been designed and constructed to image the motion of individual nanoparticles in solution. Software tools were developed to analyze this motion and calculate diffusion coefficients.

Various concentrations of fluorescent nanospheres were first imaged in water to determine if the number of detected fluorescent objects was related to the fluorescent nanospheres. The number of detected fluorescent objects decreased in proportion to the decreased concentration indicating that a direct relationship exists. However, the number of observed objects was much less than the estimated number due to two reasons: (1) there was low fluorescence in the evanescent wave, and (2) there could be repulsive interactions between the glass and the nanospheres.

Fluorescent nanospheres were also imaged diffusing in glycerol solutions at various viscosities to determine if the diffusion coefficients determined from single particle tracking are consistent with the trends predicted by the Stokes-Einstein model. The experimental diffusion coefficients were similar to those calculated from the Stokes-Einstein equation and exhibited the expected trends with viscosity, which led to the conclusion that TIRF microscope could be used to accurately measure diffusion coefficients for diffusive species in aqueous solutions.

With a few adjustments, this TIRF microscope system may be used to image protein diffusion in three dimensions both in solution and hydrogels.

6. Recommendations

There are a few recommendations for future work in order to convert the current experimental setup from the two-dimensional imaging system for nanospheres in aqueous solutions to a three-dimensional imaging system for fluorescently-labeled proteins in gels.

6.1. Prevent Adsorption on Coverslip

The images in this thesis showed a small amount of adsorption of the nanospheres and the top coverslip. As seen in Figures 4.10-4.15, the addition of glycerol appeared to prevent adsorption of the nanoparticles.

There are a few ways that could be used to prevent adsorption of the fluorescent objects. The glass cleaning procedure is performed to remove contaminants and potential surface charges. The current alkaline wash step could be changed to a cleaning step with another alkaline solution to better remove surface charges. One possible option is use oxygen plasma cleaning to remove contaminates at the surface. Preliminary studies have shown that the adsorption of Rhodamine 6G on the surface of borosilicate glass is not permanent when cleaned with argon and oxygen plasma cleaning (Appendix B). Other surface modifications, including the addition of a silicone to the coverslip surface could also prevent surface adsorption.

6.2. Observation of Particles at Shorter Exposure Times over More Image Frames

The shallow penetration depth of the evanescent wave illuminates a small amount of the sample, creating an image with a large signal-to-noise ratio (Moerner and Fromm, 2003). It also might be too small to image nanoparticles. An estimation for distance traveled in a time interval of 0.1 s ($\delta=\sqrt{4Dt}$) yielded a value of approximately 2 μm, which was much greater than the depth of the evanescent wave. The particles are likely to diffuse in the z-direction out of the evanescent wave and out of the image. Measurements at shorter exposure times will be able to

observe particles or molecules for a greater number of frames before they diffuse out of the evanescent wave. The shorter exposure times could lead to some experimental error as the EMCCD camera might be less sensitive at faster speeds.

6.3. Development of Three-Dimensional Measurements

Molecules were tracked in two dimensions with Image Pro Premier. Image Pro Premier could potentially be used analyze the axial dimension (z). The program can analyze the greyscale intensities of the particles in the image. In order to measure protein diffusion in three dimensions, a method should be determined to calibrate these greyscale intensities into particle brightness measured by the Andor Solis software. From the particle brightness, the axial position can be determined with Equation 2.4. Once this method is determined, a macro can be written into Image Pro Premier to automate the steps of this method.

6.4. Development of a Method to Image Proteins in Gels

In order to image proteins in gels, a method to place the proteins in gels needs to be developed. Thin films of polyacrylamide gels can be polymerized in between two coverslips. In Dickson et al. (1996) and Kummer et al. (1998), Nile Red and Rhodamine 6G were added to the acrylamide solution mixture prior to polymerization. We have attempted to replicate this work with Rhodamine 6G and some other proteins in these gels (Appendix C), but this procedure has not worked as the free radicals of the initiator and promoter create conjugates between the fluorescent molecules and the polymer backbone. Once the gel is polymerized and equilibrated in buffer, one coverslip could be removed from the film, and drops of the polymer solution could be added, and the coverslip could be reapplied. However, this could create pockets of buffer within the polymer film. Another method is to place the polymerized gel in the protein solution. The only concern with this method is that it might take a while for the proteins to diffuse into the

gels. A back of the envelope calculation suggests that this diffusion process might take approximately two days.

7. References

Amsden, B. (1998). Solute Diffusion within Hydrogels: Mechanisms and Models. *Macromolecules*, 31, 8382-8395.

Axelrod, D. (2001) Total Internal Reflection Fluorescence Microscopy in Cell Biology. *Traffic*, 2, 764-774.

Axelrod, D. (2007). Total Internal Reflection Fluorescence Microscopy. Török, P. and Kao, K.J. (Ed.) Optical Imaging and Microscopy: Techniques and Advanced Systems. Berlin: Springer. 195-236.

Born, M. and Wolf, E. (1999). Principles of Optics: Electromagnetic Theory of Propagation, Interference and Diffraction of Light. 7th ed. Cambridge: Cambridge.

Bos, M. and Kleijn, J. (1995). Determination of the Orientation Distribution of Adsorbed Fluorophores Using TIRF. II. Measurements on Porphyrin and Cytochrome C. *Biophys. J.*, 68, 2573-2579.

Carta, G., and Jungbauer, A. (2010). Protein Chromatography: Process Development and Scale-up. Weinheim: Wiley-VCH.

Carter, A. H. (2001). Classical and Statistical Thermodynamics. Upper Saddle River, NJ: Prentice Hall.

Cheng, N. S. (2008). Formula for viscosity of glycerol-water mixture. *Ind. Eng. Chem. Res.*, 47, 3285-3288.

Cussler, E. L. (2009). Diffusion: Mass Transfer in Fluid Systems. 3rd ed. New York: Cambridge.

Daly, S. M., Przybycien, T. M., and Tilton, R. D. (2003). Coverage-Dependent Orientation of Lysozyme Adsorbed on Silica. *Langmuir*. 19, 3848-3857.

Deich, J., Judd, E. M., McAdams, H. H., and Moerner, W. E. (2004). Visualization of the Movement of Single Histidine Kinase Molecules in Live Caulobacter Cells. *Proc. Natl. Acad. Sci.* 101, 15921-15926.

Dickson, R. M., Norris, D. J., Tzeng, Y.-L., and Moerner, W. E. (1996). Three-Dimensional Imaging of Single Molecules Solvated in Pores of Poly(acrylamide) Gels. *Science* 274, 966-968.

Douglass, A. D., and Vale, R. D. (2008). Single-Molecule Imaging of Fluorescent Proteins. Wilson, L. and Matsudaira, P. (Ed.). Methods in Cell Biology. Oxford: Elsevier. 85, 113-125.

Eghiaian, F. and Schaap, I.A.. (2011). Structural and dynamic characterization of biochemical processes by atomic force microscopy. *Methods Mol. Biol*., 778: 71–95.

Greenspan, P., Mayer, E.U., and Fowler, S.D. (1985). Nile Red: A selective fluorescent stain for intracellular lipid droplets. *J. Cell Biol*. 100: 965-973.

Jungbauer, A. (2005). Chromatographic Media for Bioseparation. *J Chromatogr. A* 1065, 3-12. 2

Kang, S. H. and Yeung, E. S. (2002). Dynamics of Single-Protein Molecules at a Liquid/Solid Interface: Implications in Capillary Electrophoresis and Chromatography. *Anal. Chem*. 74, 6334-6339.

Kang, S. H., Shortreed, M. R., and Yeung, E. S. (2001). Real-Time Dynamics of Single-DNA Molecules Undergoing Adsorption and Desorption at Liquid−Solid Interfaces. *Anal. Chem.* 73, 1091-1099.

Kuhn, J. R. and Pollard, T. D. (2005). Real-Time Measurements of Actin Filament Polymerization by Total Internal Reflection Fluorescence Microscopy. *Biophys. J.* 88, 1387-1402.

Kummer, S., Dickson, R. M., Moerner, W. E. (1998). Probing single molecules in polyacrylamide gels. Scherer, N., and Hicks, J. M. (Ed.). Proceedings of SPIE 3273, Laser Techniques for Condensed-Phase and Biological Systems, 165-173.

Lewus, R. K., and Carta, G. (1999). Protein Diffusion in Charged Polyacrylamide Gels: Visualization and Analysis. *J. Chromatogr. A* 865, 155-168.

Lichtman, J. W. and Conchello, J. A. (2005). Fluorescence Microscopy. *Nat. Methods*. 2, 910-919.

Lieto, A. M., Cush, R. C., and Thompson, N. L. (2003). Ligand-Receptor Kinetics Measured by Total Internal Reflection with Fluorescence Correlation Spectroscopy. *Biophys. J.* 85, 3294-3302.

Ma, Y, Shortreed, M. R., and Yeung, E. S. (2000). High-Throughput Single-Molecule Spectroscopy in Free Solution. *Anal. Chem.* 72, 4640-4645.

Magde, D., Wong, R., and Seybold, P. G. (2002). Fluorescence Quantum Yields and Their Relation to Lifetimes of Rhodamine 6G and Fluorescein in Nine Solvents: Improved Absolute Standards for Quantum Yields. *J. Photochem.* 75.4: 327-334.

Mattheyses, Alexa L., and Daniel Axelrod. (2006). Direct Measurement of the Evanescent Field Profile Produced by Objective-based Total Internal Reflection Fluorescence. *J. Biom. Opt.* 11, 0140061–0140067.

Moerner, W. E. and Fromm, D. P. (2003). Methods of Single-molecule Fluorescence Spectroscopy and Microscopy. *Rev. Scient. Instr.* 74, 3597-3619.

Moerner, W. E., and Orrit, M. (1999). Illuminating Single Molecules in Condensed Matter. *Science* 283, 1670-1676.

Molecular Probes. (2005). FluoSpheres Fluorescent Microspheres. Eugene, OR.

Rottenfusser, R., Wilson, E. E., and Davidson, M. W. (2014). Education in Microscopy and Digital Imaging. ZEISS Microscopy Online Campus. Accessed online at http://zeiss-campus.magnet.fsu.edu/articles/basics/psf.html.

Russell, S. M., Belcher, E. B., and Carta, G. (2003). Protein Partitioning and Transport in Supported Cationic Acrylamide-based Hydrogels. *AIChE J*. 49, 1168-1177.

Ruthardt, N., Lamb, D. C., and Bräuchle, C. (2011). Single-particle Tracking as a Quantitative Microscopy-based Approach to Unravel Cell Entry Mechanisms of Viruses and Pharmaceutical Nanoparticles. *Mol. Ther*. 19.7: 1199-1211.

Schmidt, T., Schuetz, G. J., Baumgartner, W., Gruber, H. J., and Schindler, H. (1995). Characterization of Photophysics and Mobility of Single Molecules in a Fluid Lipid Membrane. *J. Phys. Chem.* 99, 17662-17668.

Strauss E., Prekel, H., D. Otteker, D., and Reisfeld, R. (1990). Photothermal spectroscopy of Rhodamine 6G dye in organic and inorganic amorphous films. Springer Series of Optical Science. 62, 117-119.

Tanaka, T. (1981) Gels. *Sci. Am*. 244, 124-138.

Vigeant, M. A. S., Ford, R. M., Wagner, M., and Tamm, L. K. (2002). Reversible and Irreversible Adhesion of Motile Escherichia Coli Cells Analyzed by Total Internal Reflection Aqueous Fluorescence Microscopy. *Appl. and Envir. Microb.* 68, 2794-2801.

Vrljic, M, S Y. Nishimura, S. Y., and Moerner, W. E. (2007). Single Molecule Tracking. McIntosh, T. J. (Au). *Lipid Rafts*. 398. Totowa: Humana. 193-219.

Weiss, S. (1999). Fluorescence Spectroscopy of Single Biomolecules. *Science*. 283, 1676-1683.

Xu, X-H. and Yeung, E. S. (1997). Direct Measurement of Single-Molecule Diffusion and Photodecomposition in Free Solution. *Science* 275, 1106-1109.

Appendix A: Total Internal Reflection Fluorescence Microscope Protocol

A.1. Coverslip Cleaning Procedure

This section describes the procedure for cleaning the coverslips for the work with nanospheres. It is believed that this procedure will need to be revised for work with proteins (Recommendations section 6.1)

1. Make a 0.2 M solution of NaOH (approximately 0.7 g in 100 mL)
2. Place coverslips on the plastic coverslip holder (shown in Figure A-1).
3. Pour 70-80 mL of NaOH solution into 100 mL beaker, and then place the coverslips and coverslip holder into solution (shown in Figure A-1).
4. Sonicate the coverslips for 15 minutes.
5. Sonicate the coverslips for 5 minutes in water. Perform three times.
6. Dry coverslips with Helium gas.

Figure A-1. Plastic coverslip holder used for cleaning and storing coverslips.

A.2. Setting up the Andor Solis Software

The procedure for setting up the Andor Solis software for data acquisition is as follows:

1. Open the Andor Solis program.

2. Close the shutter of the camera by clicking on the “Shutter Control” button and then closing the internal and external shutter. Keep the shutter closed until the room lights are off, and the sample is ready for imaging.
3. Click on the “Setup Acquisition” button.
    a. Set the Acquisition Mode to Kinetic.
    b. Set the Exposure Time to 0.100 s.
    c. Set the Kinetic Series Length to 100 for 100 images
    d. Click on the “OptAcquire Menu” button
        i. Click on “Sensitivity and Speed (EM Amplifier)” and then click ok.
    e. Check that the EM Gain is set to 300 and click Ok.
4. The temperature of the CCD camera, shown in the box on the bottom left corner, should be cooling to -75°C. When the camera isn’t at -75°C, the box will be red. When it reaches -75°C, the box will be blue. To set the temperature, click on the box, set the temperature and click “Ok”.
5. Now the software is ready for imaging. Once the sample is on the stage and ready for imaging, open the camera lens by clicking on the “Shutter Control” button and then opening the internal and external shutter.

A.3. Microscope Alignment Procedure

A.3.1. Laser Start-up Procedure

Note: As of the writing of this thesis, the laser is set up, so steps 1 and 2 should be complete, but it is worth checking.

1. Mount the laser to the optical table by mounting the laser to a metal plate with washers and screws.
2. Connect the laser head to power supply. Make sure the serial numbers of the laser and power supply are the same.
3. Connect the remote interlock and TTL signal to the power supply. See page 8 of User Manual for correct placement of pins.
4. Turn the master key switch to the OFF position.
5. Connect the power cord to the power supply. Check the line voltage before plugging the power cord into the electrical power source. Make sure it is the same as the voltage indicated on the back panel of the laser supply.
6. Turn on the main power switch. The POWER ON indicator light should go on. Allow the laser to start to warm up for 30 seconds before proceeding to the next step.
7. Manually open the aperture shutter.
8. Turn on the master key switch. After a >30 second delay, the master key switch can be turned on. The LASER ON indicator light should go on. In this state, the laser can emit a good quality beam from the aperture after the laser warms up.

A.3.2. Beam Alignment Procedure

This alignment procedure has been adapter for this microscope from Axelrod (2007).

1. Mount the prism on the microscope stage or optical table.
2. Prepare the path for the laser with mounts for the focusing lens and collimator.
3. Place a coverslip with a uniform dried spread of fluorescent dye in the same type of sample holder to be used for experiments.

4. Place a small droplet of immersion oil on the non-DiI surface of the sample coverslip and carefully translate the prism vertically so it touches and spreads the oil.
5. With safety glasses and without any focusing lens in place, adjust the unfocused collimated laser beam position with the mirrors so that total internal reflection occurs directly in line with the objective's optical axis, which can be seen by observing the scattering of the laser light as it travels through the prism, oil, and the total internal reflection surface.
6. Insert the focusing lens so that the focus is roughly at the total internal reflection interface under observation. Adjust the lateral position with micrometer screws on the focusing lens mount so that the total internal reflection region occurs directly in line with the objective. To guide this adjustment, look for three closely aligned spots of scattered light, corresponding to where the focused beam first crosses the immersion oil layer, where it totally reflects off the sample surface, and where it exits by crossing the oil again.
7. The total internal reflection region should now be positioned well enough to appear in the view of the microscope when seen as fluorescence with the standard filters in place. In general, the total internal reflection region will appear as a yellow ellipse or streak. Make final adjustments with the focusing lens to center this area. The focusing lens can be moved forward or backward along the laser optical path to achieve the desired size of the total internal reflection area.

A.4. Imaging Procedure

1. After aligning the microscope, place a drop of immersion oil on objective.

2. Place the sample in between two coverslips by placing a 10 μm droplet on one coverslip and then sandwich the sample droplet with the other coverslip, creating a thin film of liquid between two coverslips.
3. Place the sample on the microscope stage above the objective.
4. Place a drop of immersion oil on the top coverslip.
5. Lower prism to touch oil, but not push down on coverslip sample. The sample should be able to move along with the microscope stage.
6. Turn on the laser and the camera by selecting "Video".
7. Slowly scan the image in the z-direction for fluorescent objects of interest with the fine focus.
8. Click on the "Take image" button when you want to take an image of the sample.
9. To remove a sample, lift up the prism, remove the sample from the microscope. Clean off the immersion oil from the bottom of the prism and the objective with lens cleaning paper.

A.5. Shut Down Procedure

A.5.1. Laser Shut-Down Procedure

To shut down the laser, use the master key switch to turn off laser and then turn off the main power switch.

A.5.2. Convert TIF Files into SIF Files

Once all of the images have been taken, the images first need to be converted into TIF files for further evaluation and analysis. Simply resave the files as TIF files by selecting an

image and selecting “Save As”. Then select “All frames”, “Entire Images”, and “8-bit” to save all of the entire images as 8-bit TIF images.

A.5.3. Cleaning the Microscope

1. Lift the prism holder and remove the sample. The sample can be thrown away.
2. Remove the prism from the prism holder. Apply a drop of optical lens cleaning solution to a lens paper. Do not use a kinwipe. Clean the prism with the wet lens paper and dry it with a dry piece of lens paper.
3. Apply a drop of optical lens cleaning solution to a lens paper. Do not use a kinwipe. Clean the objective lens with the wet lens paper and dry it with a dry piece of lens paper.
4. Cover microscope with cover to prevent dust build-up.

A.6. Image Pro Plus Procedure

Once the files have been converted into TIF files and are saved on the lab computer

A.6.1. Counting Fluorescent Objects

1. Open Image Pro Premier.
2. Select the “Count/Size” tab.
3. On the upper right part of the screen, manually adjust the threshold with image histogram on the right, so all the particles are highlighted and identified from the background.
4. Make sure there is a green checkmark in the “Range” button. Click the “Edit range” button. In the upper left hand side of the window, select “Range: Area”, and type in 3 for the minimum range. The program will now count all objects that are equal or greater than 3 pixels.

5. Click the “Count” button to count the images in that frame. To do this for all frames, click the arrow below “Count” and click “Count All Frames”. All objects in all of the frames for all images should be now counted.

A.6.2. Identifying Fluorescent Objects’ Trajectories

1. Open Image Pro Premier.
2. Click on the “Measure” tab.
3. Click on the “Objects” button, which will bring up a new menu bar.
4. Click the “Bright” button. Manually adjust the threshold with image histogram on the right, so all the particles are highlighted and identified from the background.
5. Click “Learning” button and then click on a diffusing particle or molecule in subsequent images. Click “Close Track” and the program will determine the length and randomness of the particles’ pathway in the image.
6. Click “Auto All” to identify particles or molecules in the image. Click “Ok” and the center of masses of all the particles or molecules in each frame will be determined in the two-dimensional plane.
7. Click “Data Table” button to generate a data table of objects and positions.
8. Click on the “Excel” button to generate the data in an Excel table.
9. Save Excel sheet in the MATLAB folder.

A.7. Procedure for Measuring Diffusion Coefficients with MATLAB

1. Open AcquiringTrajectoriesandCalculatingDiffusionCoefficients.m in Matlab.
2. On line 14 of the m-file, insert the name of the Excel file with the time positions.
3. Edit the inputs on lines 16-19 if necessary.

4. Click Run. The Diffusion Coefficient and the MSD vs Time Interval plot should now both appear in the window.

A.8. Refractive Index Measurement

The refractive index can be measured with the Abbe Refractometer (Reichert, Depew, NY) found in the undergraduate UO Lab in Wilsdorf 301. Contact Mr. Eric Anderson if you would like to use it. Typically, the lab isn't available in the afternoons, so plan on making these measurements in the morning. You may have to borrow a key from the secretaries if Mr. Anderson isn't available.

Appendix B. Work with Rhodamine 6G Molecules

B.1. Introduction

The overall goal of this project is to measure the three-dimensional diffusion of fluorescently-labeled proteins in interacting polyacrylamide gels with changes in polymer characteristics and solution properties. Achieving this goal will require a series of experiments with progressively more difficult imaging conditions.

The challenge with imaging proteins instead of the nanoparticles used in this work is three-fold. First, proteins typically carry fewer fluorescent labels than the nanospheres. The nanospheres contain on the order of 10^2 fluorescence equivalents per nanosphere, whereas proteins are usually covalently bonded to only a few fluorescent probes. The intensity of proteins will be significantly smaller than the nanospheres, so the proteins will be more difficult to image. Secondly, the proteins are smaller than the nanospheres with monoclonal antibodies having a diameter of approximately 10 nm. Finally, with a smaller size, the protein diffusion coefficient will be larger, making it more difficult to track the movement of the molecules.

This appendix describes the initial experiments performed with Rhodamine 6G, which should be even more challenging than imaging proteins, due to a smaller size and faster diffusion.

B.2. Materials and Methods

B.2.1. Materials

B.2.1.1. Rhodamine 6G

Rhodamine 6G was purchased from Sigma Aldrich. The structure of Rhodamine 6G is shown in Figure B-1. All other laboratory chemicals used were from Fischer Scientific (Pittsburgh, PA). The coverslips and TIRF microscope were the same as described in the Materials and Methods sections 3.2.1 and 3.2.4, respectively.

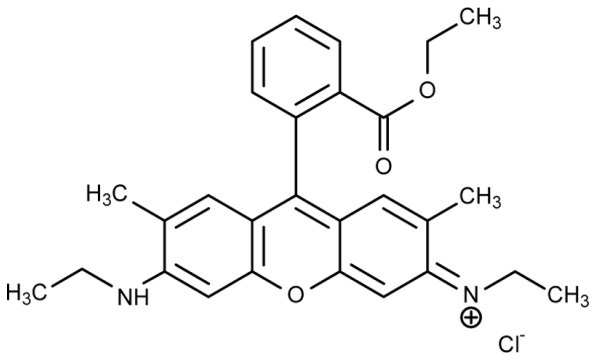

Figure B-1. Structure of Rhodamine 6G (Magde et al., 2002).

B.2.1.2. Buffers

Phosphate buffers were prepared using dibasic sodium phosphate (Na_2HPO_4) phosphoric acid at pH 7. The buffer solutions that contained sodium chloride were prepared by first adding sodium chloride and then titrating with the correct acid to the desired pH. All chemicals used in this study were analytical reagent grade and were obtained from Fisher Scientific.

B.2.2. Methods

B.2.2.1. Cleaning Coverslips

Coverslip cleaning was performed with two different methods: the alkaline cleaning steps performed in Section 3.2.1 and oxygen plasma cleaning.

B.2.2.1.1. Oxygen Plasma Cleaning

Since Rhodamine 6G is known to adsorb very substantially on glass coverslips, the coverslips were treated with argon and oxygen plasma cleaning (Strauss et al., 1990). Plasma gas removes organic materials and other contaminants while minimizing etching of the glass coverslips. Plasma cleaning was performed with the Model PC 2000 Plasma Cleaner (South Bay Technology, Inc., San Clemente, CA). The sample chamber was loaded with the coverslip samples at room temperature. Argon was first flowed into the sample chamber at a pressure of less than 200 milliTorr for 5 minutes. Then the oxygen gas was flowed into the sample chamber at a pressure of less than 200 milliTorr for 5 minutes. For both gases, the Radio Frequency (RF) Forward Power was set to 10 W and the RF Reflected Power was set to 0 W.

B.2.2.2. TIRF Microscopy

As an initial experiment to detect fluorescence of Rhodamine 6G in solution, Rhodamine 6G was diluted in solution. A 10 μL sample was placed between two coverslips. This sandwich was placed in the TIRF microscope and imaged with a laser incident angle of 72 degrees, which gave an estimated evanescent wave penetration depth of 125 nm. All other TIRF microscopy imaging properties were the same as the properties presented in Materials and Methods sections 3.2.4 through 3.2.7.

B.3. Results

B.3.1. Images of Rhodamine 6G with Alkaline-Cleaned Coverslips

A solution of 1.0×10^{-6} g/L (2.1×10^{-9} M) of Rhodamine 6G molecules in 20 mM H_2PO_4 and 200 mM NaCl at pH 7 was imaged with the TIRF microscope. An image of the Rhodamine 6G sample is shown in Figure B-2, and a series of twelve consecutive enhanced images is shown in Figure B-3. The molecules were mostly permanently adsorbed on the surface of the coverslip. The few molecules that were only temporarily adsorbed quickly diffused out of the evanescent wave within one time step (0.100 seconds). Thus, no significant position measurements and diffusivity calculations were made. This result shows that another coverslip cleaning method is necessary to prevent adsorption of the Rhodamine 6G molecules in solution.

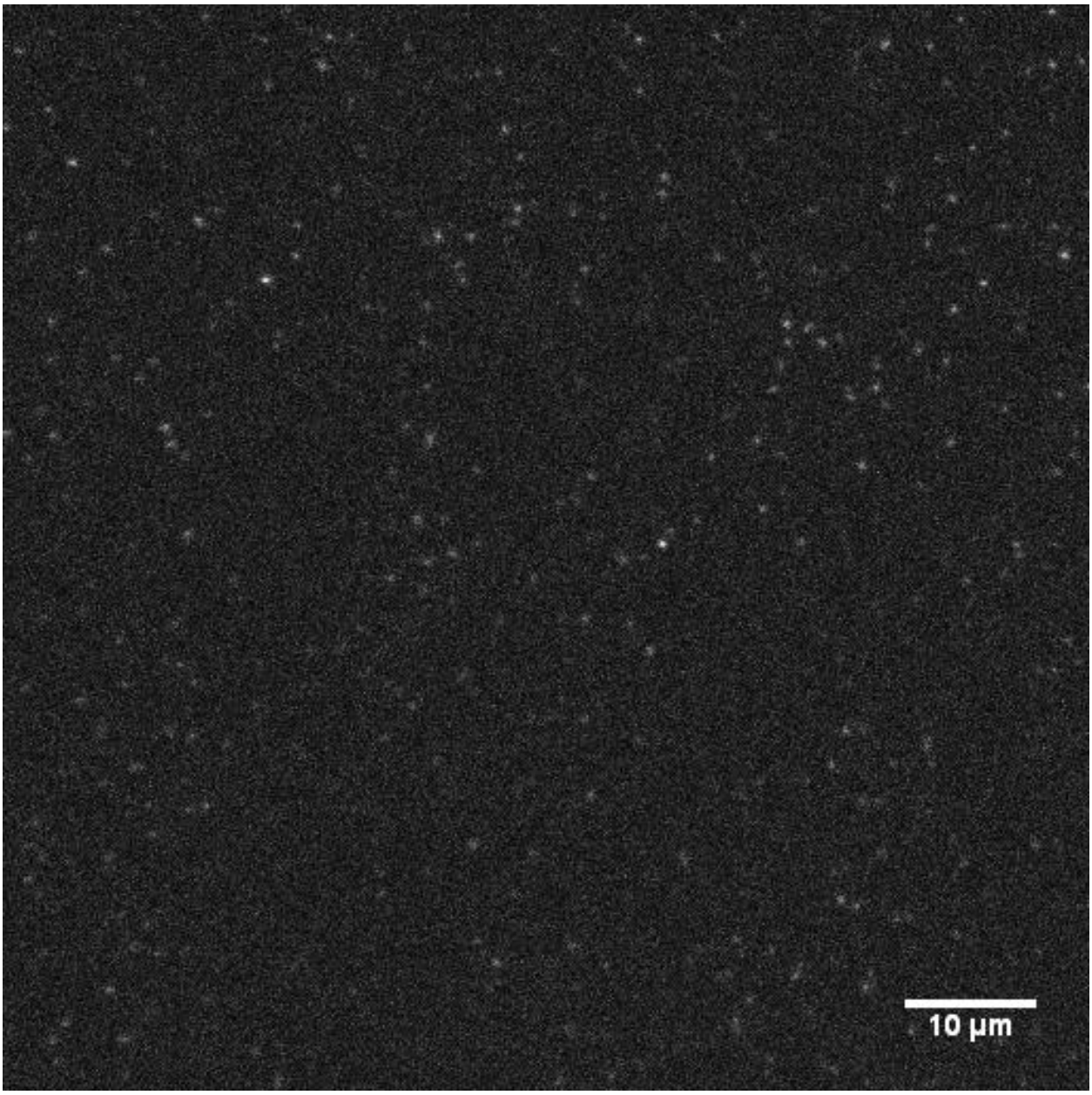

Figure B-2. TIRF microscopy image of Rhodamine 6G molecules at a concentration of 1.0 x 10^{-6} g/L (2.1 x 10^{-9} M) in 20 mM H_2PO_4 and 200 mM NaCl at pH 7.

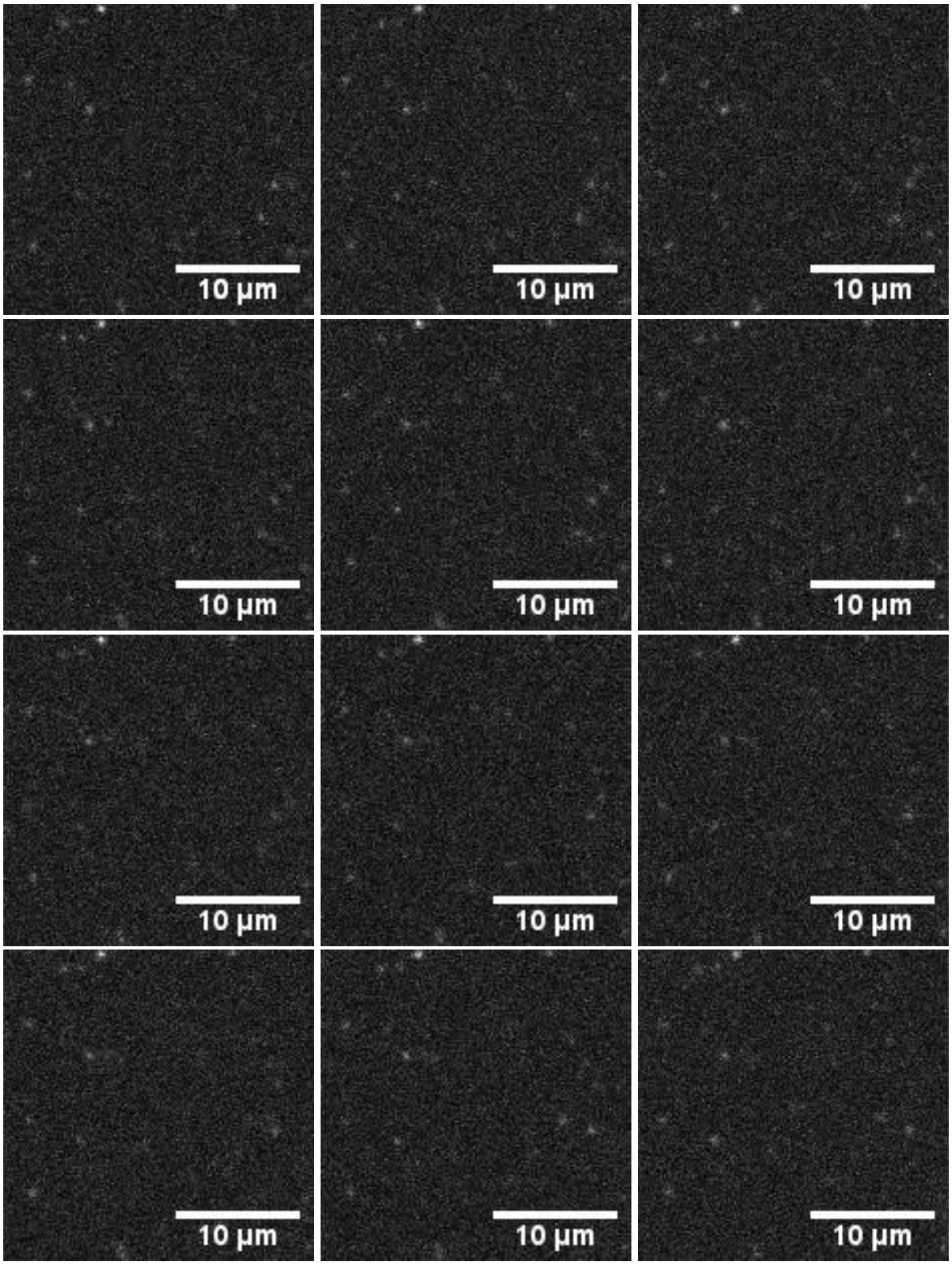

Figure B-3. Twelve consecutive TIRF microscopy images of Rhodamine 6G molecules at a concentration of 1.0×10^{-6} g/L (2.1×10^{-9} M) in 20 mM H_2PO_4 and 200 mM NaCl at pH 7.

B.3.2. Images of Rhodamine 6G with Plasma-Cleaned Coverslips

After the coverslips were plasma-cleaned, a solution of 4.0×10^{-6} g/L (8.4×10^{-9} M) of Rhodamine 6G molecules in 20 mM H_2PO_4 and 200 mM NaCl at pH 7 was imaged with the TIRF microscope. Figure B-4 shows an image of the Rhodamine 6G sample and Figure B-5 shows a series of twelve consecutive images of this sample.

There are two major differences between the results from the plasma-cleaned coverslips and the alkaline-cleaned coverslips. There were fewer molecules that adsorbed to the glass surface with the plasma-cleaned coverslips (Figure B-4) than the alkaline-cleaned coverslips (Figure B-2). The adsorption was mostly temporary with the plasma-cleaned coverslips, rather than mostly permanent with the alkaline-cleaned coverslips. Similar to the alkaline-cleaned coverslips, the molecules diffused out of the evanescent wave after one time step, so no position measurements and diffusivity calculations were made.

This work shows that the adsorption of Rhodamine 6G on the surface of borosilicate glass is not permanent when cleaned with argon and oxygen plasma cleaning.

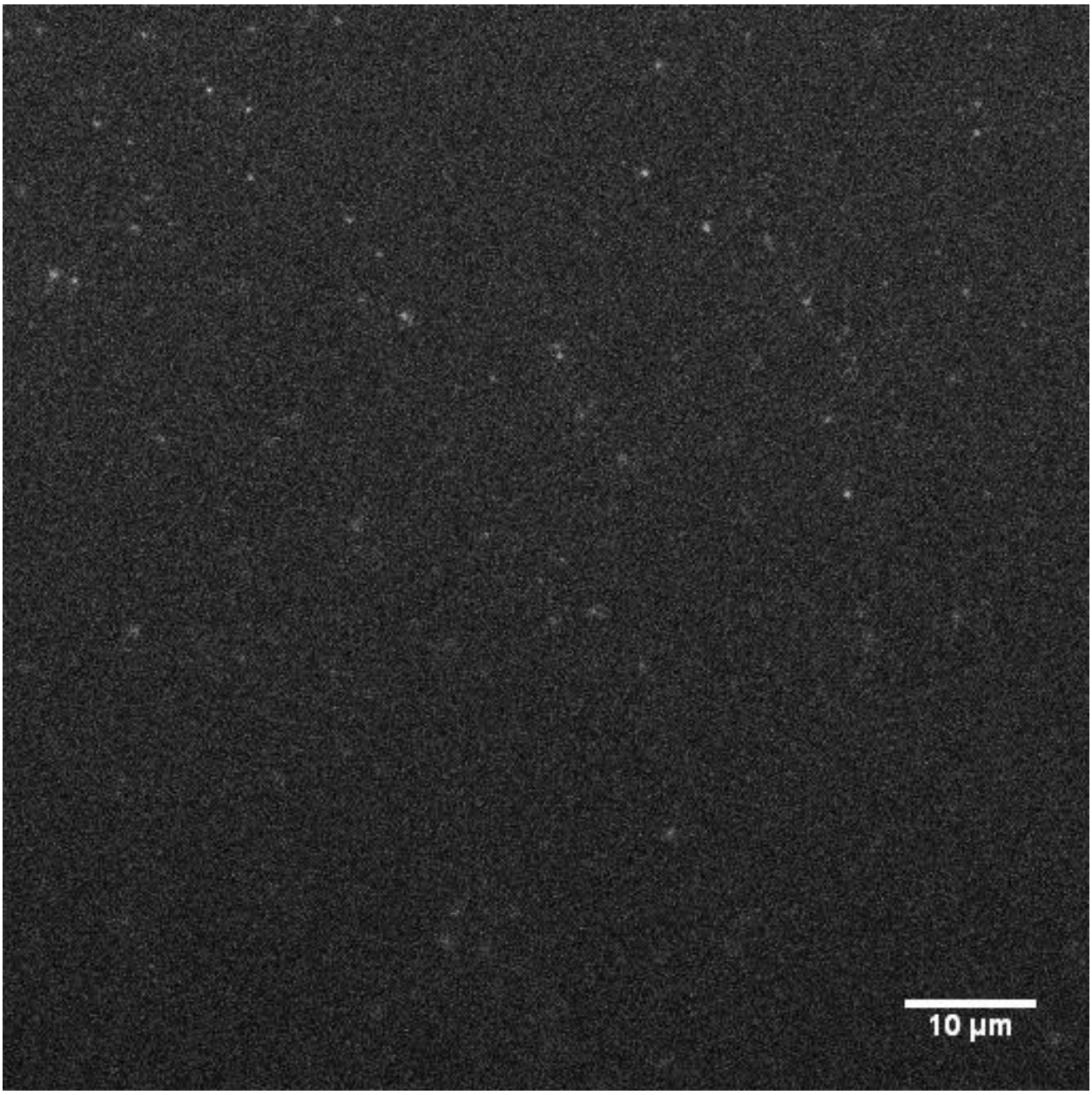

Figure B-4. TIRF microscopy image of Rhodamine 6G molecules at a concentration of 4.0 x 10^{-6} g/L (8.4 x 10^{-9} M) in 20 mM H_2PO_4 and 200 mM NaCl at pH 7. The coverslips were cleaned with plasma cleaning prior to imaging.

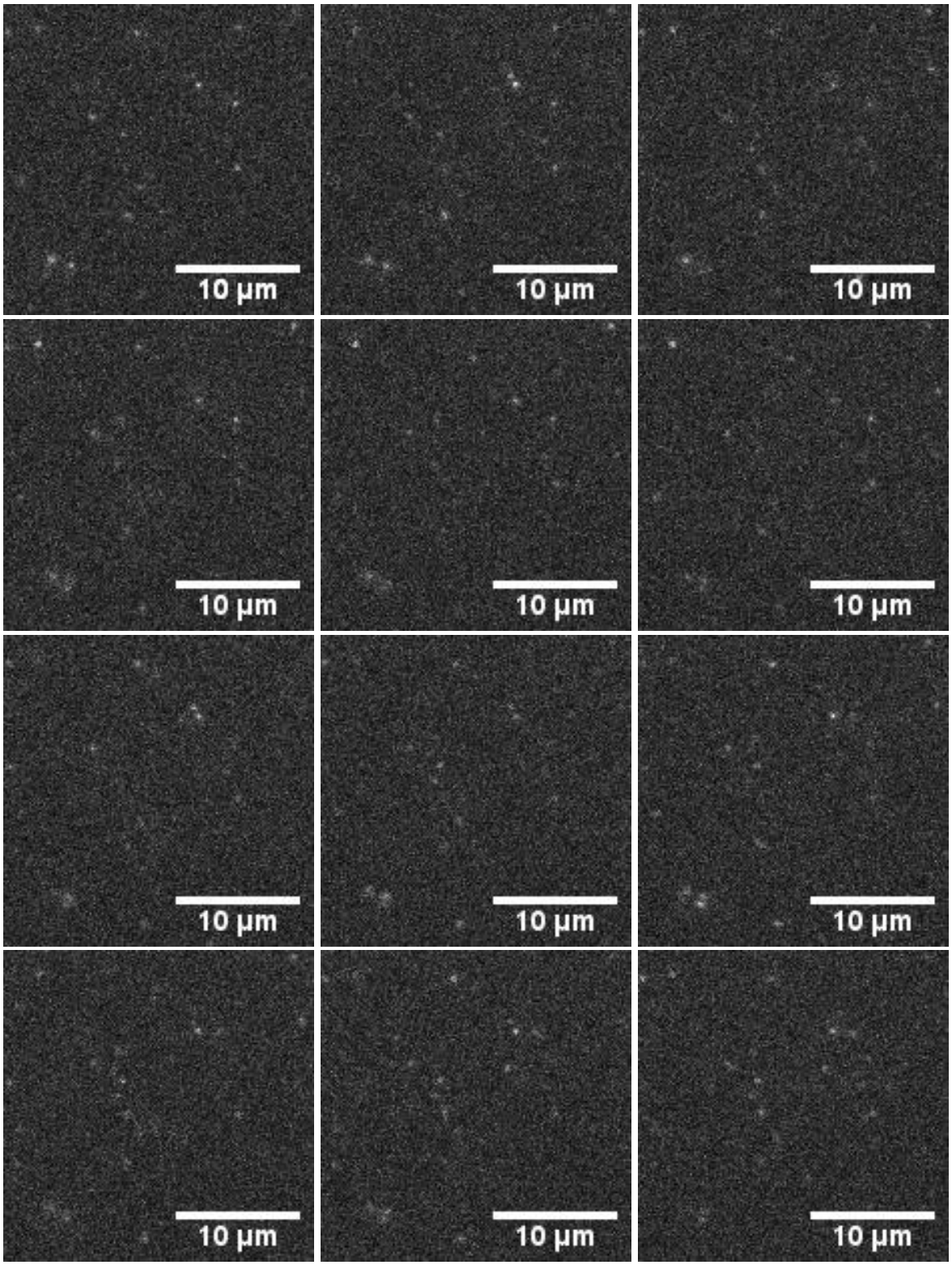

Figure B-5. Twelve consecutive TIRF microscopy images of Rhodamine 6G molecules at a concentration of 4.0 x 10^{-6} g/L (8.4 x 10^{-9} M) in 20 mM H_2PO_4 and 200 mM NaCl at pH 7. The coverslips were cleaned with plasma cleaning prior to imaging.

Appendix C. Work with Polyacrylamide Gels

C.1. Introduction

The overall goal of this project is to measure the three-dimensional diffusion of fluorescently-labeled proteins in interacting polyacrylamide gels with changes in polymer characteristics and solution properties. Lewus and Carta (2001) studied the diffusion and partitioning of cytochrome c, a cationic protein during experimental conditions, in an anionic polyacrylamide-based hydrogel in square capillary tubes. The procedure used in their report to fill the capillary tubes with polyacrylamide gels was manipulated for placing the gels between two coverslips. The work in this appendix is a sampling of the work performed with polyacrylamide gels.

C.2. Materials and Methods

C.2.1. Materials

The monomers used in the preparation of the polyacrylamide gels were neutral acrylamide (99% purity) and the negatively-charged 2-acrylamido-2-methylpropane sulfonic acid (AMPS, 98% purity). N,N′-Methyl bisacrylamide (MBA, 98% purity), ammonium persulfate (AP, 98% purity), and N,N,N′,N′-Tetramethylethylenediamine (TEMED, 99%) were used as the crosslinker, initiator, propagator, respectively. Bind-silane (3-Trimethoxysilylpropyl methacrylate) was used to bind the gel to the coverslip surface. All of these chemicals were obtained from Sigma Aldrich. The 28 nm fluorescent nanospheres used are described in Section 3.3.1 of Materials and Methods. Rhodamine 6G and fluorescein were purchased from Sigma-Aldrich (St. Louis, MO). All other laboratory chemicals used were from Fischer Scientific (Pittsburgh, PA).

The coverslips and TIRF microscope were the same as described in the Materials and Methods in sections 3.2.1 and 3.2.4, respectively.

C.2.2. Methods

C.2.2.1. Bind-silane Coating

The bind-silane solution was made by adding acetic acid to the 100 mL of distilled water to lower the pH to 3.5. Then 0.4 mL of bind-silane was added. This solution was stirred for 15 minutes to eliminate any emulsions. The coverslips, cleaned according to the procedure in section 3.2.1 of the Materials and Methods, were submerged in this solution for 60 minutes and then rinsed in distilled water before air drying for 60 minutes.

C.2.2.2. Polymerization Reaction

The following procedure is the formulation to polymerize 10 mL of a polyacrylamide gel with a 5% cross-link density (mass of crosslinker/mass of monomer), 0.21 g/mL polymer concentration (mass of monomer and crosslinker/volume of final gel product), and a charge density of 970 μeq/mL (1 μeq = 1 μmol of charge). The polymerization reaction is shown in Figure C-1.

First, 2.0 g of acrylamide and 0.1 g of MBA were mixed with 5 mL of distilled water. Additional distilled water was added to the mixture to increase the volume to 10 mL. This solution was degassed with helium gas for 15 minutes. To promote polymerization, 0.005 g of AP and 10 μL of TEMED were added to the reaction mixture. The reaction mixture was rapidly mixed and a 10 μL droplet was added to one coverslip coated with bind-silane. Another bind-silane coated coverslip was sandwiched on top of the gel, forming a soft gel layer. This reaction

mixture would polymerize in a film in between two coverslips. The polymerization reaction ended approximately after one hour, which was identified by the lack of heat released from the polymerization reaction.

For negatively charged polyAMPS gels, NaOH (~0.91 mL of 11 M NaOH) was added to the mixture until pH was between 6 and 8 prior to any polymerization.

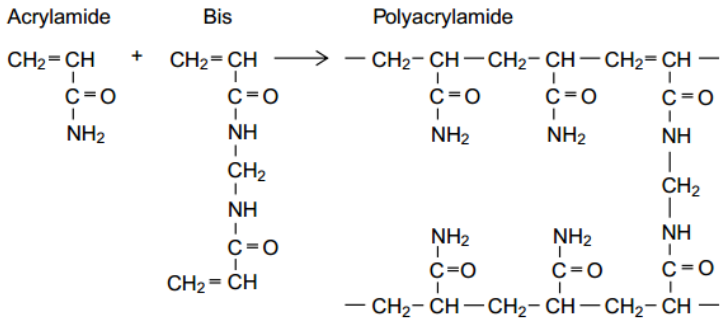

Figure C-1. Polymerization reaction of polyacrylamide gel.

The refractive index of the gel was measured with the Abbe Refractometer (Reichert, Depew, NY). The refractive index of the polyacrylamide gel was determined to be 1.37.

C.2.2.3. Microscopy Techniques

C.2.2.3.1. Epifluorescence

One of the important characteristics of the polyacrylamide gels is that the gel film is homogeneous. To determine if the polymerization of the gel was homogeneous, fluorescently-labeled gels would be imaged with an epifluorescent microscope.

To label the neutral polyacrylamide gels, 0.2 mg of Rhodamine 6G was added to the polymerization mixture. To label the anionic polyAMPS gels, 0.02 g of fluorescein was added to

the polymerization mixture. These solutions were placed in between coverslips to create a thin film as described in section C.2.2.2.

These samples were imaged with the Nikon Eclipe E200 epifluorescent microscope at 10x magnification with a similar setup used previously (Russell et al., 2003). A mercury lamp was used to visually the fluorescent molecules. The filter set of 528-553 nm for excitation, 565 nm for the dichroic mirror, and 600-660 nm barrier filter was used for the Rhodamine 6G labeled polyacrylamide gel samples. For the fluorescein labeled polyAMPS gel samples, the filter set of 450-490 nm for excitation, 500 nm for the dichroic mirror, and 515 nm barrier filter was used. Images were captured with a Sanyo Hi-Resolution CCD camera interfaced to a Dell desktop computer. The gel samples were scanned in one direction in an attempt to detect any heterogeneities.

C.2.2.3.2. TIRF Microscopy

As an initial experiment to detect fluorescence in gels, 28 nm fluorescent nanospheres were imaged in the polyacrylamide gels. The incident angle was set to 72 degrees, which gave an estimated evanescent wave penetration depth of 190 nm. All other TIRF microscopy imaging properties were the same as the properties presented in Materials and Methods sections 3.2.4 through 3.2.7.

C.3. Results

C.3.1. Homogeneity of Polyacrylamide Gel Films

Epifluorescent images were taken of polyacrylamide and polyAMPS gels loaded with fluorescent labels. The epifluorescence images of both gel samples are shown in Figure C-2. In the interior of the coverslips, the gels are completely saturated with fluorescent labels. Therefore, both the polyacrylamide and polyAMPS gels are homogeneous throughout, since there are no air bubbles or other heterogeneities within the gels.

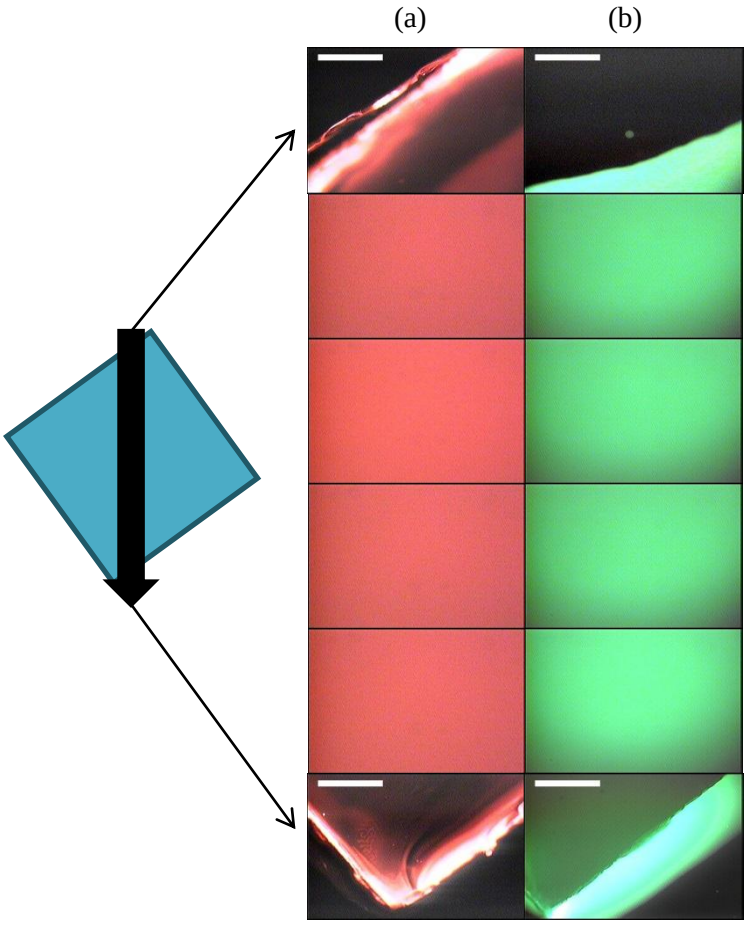

Figure C-2. Epifluorescent images of (a) Rhodamine 6G labeled polyacrylamide gels and (b) fluorescein labeled polyAMPs gels. Scale bar is 50 μm.

C.3.2. TIRF Microscopy Images in Polyacrylamide Gels

C.3.2.1. Images of 28 nm Nanospheres

To detect fluorescence in gels, 28 nm fluorescent nanospheres were imaged in the polyacrylamide gels. The polyacrylamide gel was a 10.5 g/mL polymer and 5.0% crosslinker. A concentration of 2.0×10^{-6} g/mL of nanospheres was added to the polymerization mixture prior to polymerization. The incident angle was 72 degrees, which gave an estimated evanescent wave penetration depth of 190 nm. All other TIRF microscopy imaging properties were the same.

An image of the 28 nm particles in PAA gel is shown in Figure C-3. The particles were unable to freely diffuse throughout the gel. The nanoparticles were either covalently connected to the polyacrylamide gel or were contained within pores of the gel, which are much smaller than 28 μm. This result shows that the TIRF microscopy setup can image fluorescence in polyacrylamide gels.

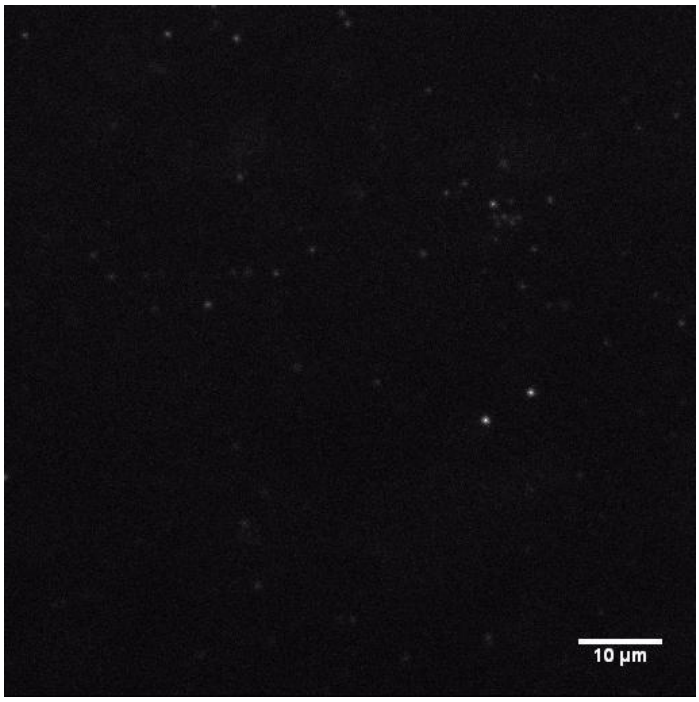

Figure C-3. TIRF microscopy image of 28 nm nanospheres in 10.5% polyacrylamide gels with a 5.0% crosslinker.

C.3.2.2. Images of Rhodamine 6G

To detect fluorescence of smaller fluorescent molecules in gels, individual Rhodamine 6G molecules were imaged in a 21% polymer polyacrylamide gel with 5.0% crosslinker. The gel layer in between two coverslips was equilibrated in 10 mM Sodium Acetate buffer with 100 mM NaCl buffer at a pH of 5.0 for 24 hours. Then the top coverslip was removed and gel layer was placed in a solution of 1.2×10^{-5} mg/mL of Rhodamine 6G for 1 minute.

An image of Rhodamine 6G in polyacrylamide gel is shown in Figure C-4. Molecules were seen diffusing around in pockets approximately 10 µm in size within the image. The pockets are either polyacrylamide gel or liquid filled pores that were generated when the top coverslip was removed from the gel film. To characterize the media, the diffusion coefficient of

the molecules could be determined from Brownian motion (Equation 2.18). Since the diffusion coefficients in the thesis work were relatively accurate, then could calculate the viscosity using Stokes-Einstein (Equation 2.6) and compare it to the viscosity of polyacrylamide gel and buffer. However, the molecules are too dense to confidently measure trajectories and calculate diffusion coefficients.

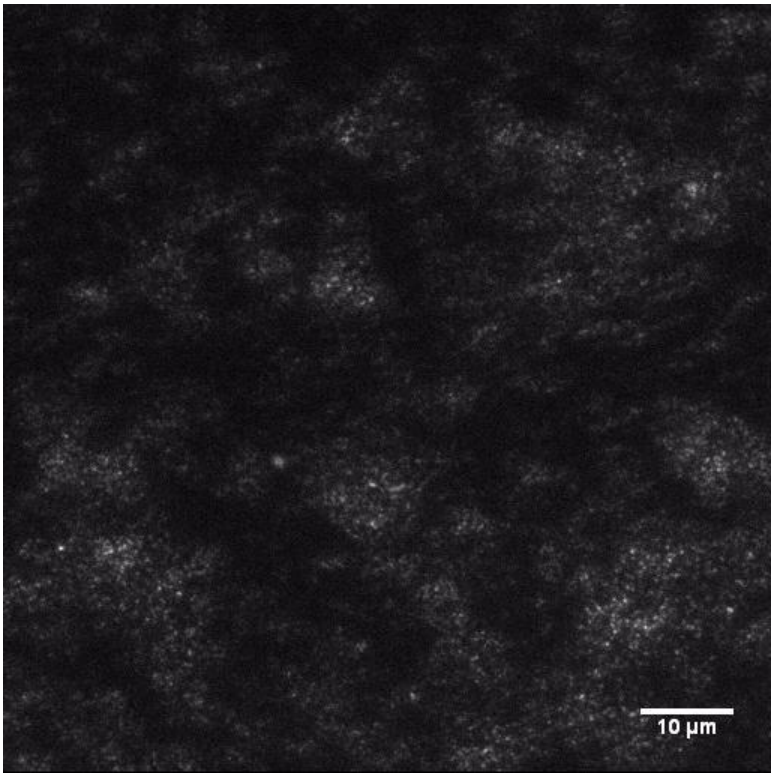

Figure C-4. TIRF microscopy image of Rhodamine 6G in 21% polyacrylamide gels with a 5.0% crosslinker.